J Mar Sci Technol (2013) 18:471–496
DOI 10.1007/s00773-013-0221-6

ORIGINAL ARTICLE

Investigation of water depth and basin wall effects on KVLCC2 in manoeuvring motion using viscous-flow calculations

S. L. Toxopeus · C. D. Simonsen · E. Guilmineau · M. Visonneau · T. Xing · F. Stern

Received: 2 October 2012 / Accepted: 31 March 2013 / Published online: 11 May 2013

Abstract The objective of the NATO AVT-161 working group is to assess the capability of computational tools to aid in the design of air, land and sea vehicles. For sea vehicles, a study has been initiated to validate tools that can be used to simulate the manoeuvrability or seakeeping characteristics of ships. This article is part of the work concentrating on manoeuvring in shallow water. As benchmark case for the work, the KVLCC2 tanker from MOERI was selected. At INSEAN, captive PMM manoeuvring tests were conducted with a scale model of the vessel for various water depths. Several partners in the AVT group have conducted RANS calculations for a selected set of manoeuvring conditions and water depths for the bare hull. Each partner was asked to use their best practice and own tools to prepare the computations and run their flow codes. Specific instructions on the post-processing were given such that the results could be compared easily. The present article discusses these results. Detailed descriptions of the approach, assumptions, and verification and validation studies are given. Comparisons are made between the computational results and with the experiments. Furthermore, flow features are discussed.

Keywords KVLCC2 · Viscous flow · Manoeuvring · Shallow water · Wall effects

S. L. Toxopeus (✉)
Maritime Research Institute Netherlands (MARIN)/Delft University of Technology, Wageningen, The Netherlands
e-mail: s.l.toxopeus@marin.nl

C. D. Simonsen
FORCE Technology, Lyngby, Denmark
e-mail: cds@force.dk

E. Guilmineau · M. Visonneau
ECN-Ecole Centrale de Nantes, Nantes, France
e-mail: Emmanuel.Guilmineau@ec-nantes.fr

M. Visonneau
e-mail: Michel.Visonneau@ec-nantes.fr

T. Xing
University of Idaho, Moscow, ID, USA
e-mail: xing@uidaho.edu

F. Stern
IIHR-Hydroscience and Engineering, The University of Iowa, Iowa City, IA, USA
e-mail: frstern@engineering.uiowa.edu

1 Introduction

The NATO Specialist Team in Naval Ship Manoeuvrability (ST-NSM) is developing a Standardization Agreement (STANAG) regarding common manoeuvring capabilities for NATO warships for specific missions. The naval ships are subject to more strict criteria than imposed by IMO resolutions for commercial vessels, as explained by Örnfelt [1]. To verify compliance with the STANAG, high-fidelity predictions of the ship's manoeuvring characteristics are required. In Quadvlieg et al. [2] it was concluded that modern empiric prediction tools have not been validated thoroughly for all possible manoeuvres or missions described in the STANAG and therefore further validation and improvements are required. The objective of the NATO AVT-161 working group is to assess the capability of computational tools to aid in the design of air, land and sea vehicles. If these tools prove to be accurate in prediction of these characteristics, they can be used to obtain more accurate assessments of compliance with the STANAG. For sea vehicles, a study has been initiated to validate tools that can be used to simulate the manoeuvrability or seakeeping

Table 1 Main particulars of the KVLCC2

Description	Symbol	Magnitude		Symbol
		Ship	Model	
Length between perpendiculars	L_{pp}	320	7.00	m
Moulded breadth	B	58	1.269	m
Moulded draught	T	20.8	0.455	m
Displacement volume moulded	Δ	312635	3.273	m^3
Wetted surface area bare hull	S_{wa}	27197	13.01	m^2
Position centre of buoyancy forward of midship	x_B	3.50	0.077	m

characteristics of ships. This article is part of the work concentrating on manoeuvring in shallow water. In the present study, the capability to predict the influence of the water depth on the forces and moments on a ship will be investigated. In Simonsen et al. [3], the importance of the domain width for shallow water conditions was already stressed and it was suggested that blockage may contribute to the scatter in the results from different towing tanks for the *Esso Osaka*. Therefore, special attention will be paid to the effect of the blockage on the results.

As benchmark case for the work, the KVLCC2 tanker from MOERI was selected. At INSEAN, captive PMM manoeuvring tests were conducted in 2005/2006 with a 7 m scale model of the vessel (scale: 1:45.714) for various water depths. The main particulars of the KVLCC2 are given in Table 1. Several partners in the AVT group have conducted RANS calculations for a selected set of manoeuvring conditions and water depths for the bare hull. Each partner was asked to use their best practice and own tools to prepare the computations and run their flow codes. Specific instructions on the post-processing were given such that the results could be compared easily. The present article discusses these results. Detailed descriptions of the approach, assumptions, and verification and validation studies are given. Comparisons are made between the computational results and with the experiments. Furthermore, flow features are discussed.

2 Coordinate system

The origin of the right-handed system of axes used in this study is located at the intersection of the water plane, midship and centre-plane, with x directed forward, y to starboard and z vertically downward. The forces and moments are also given according to this coordinate system. Sinkage is positive for the ship moving deeper into the water and trim is positive for bow up.

In the present calculations, a positive drift angle β corresponds to the flow coming from port side (i.e. $\beta = \arctan -v/u$, with u the ship-fixed velocity in x direction and v the ship-fixed velocity in y direction). The non-dimensional yaw rate γ is calculated with $\gamma = r \times L_{pp}/V$ and is positive for a turning rate r to starboard when sailing at positive forward speed V.

3 KVLCC2 model tests

The KVLCC2 (KRISO Very Large Crude Carrier) hull form was one of the subjects of study during the CFD Workshops Gothenburg 2000 [4] and 2010 [5] and the SIMMAN 2008 Workshop [6]. For straight ahead conditions, the flow features and resistance values were measured, see Lee et al. [7] and Kim et al. [8].

Captive model tests for the bare hull KVLCC2 were conducted by INSEAN in 2005/2006 in preparation for the SIMMAN 2008 Workshop [6], see also Fabbri et al. [9–11]. The scale of the ship model, INSEAN model no C2487, was 1:45.71. A set of PMM tests comprising amongst others the measurement of the forces and moments for steady drift motion and oscillatory yaw motion was performed. During the tests, the model was free to heave and pitch. For the present work, only the tests with the bare hull form and a model speed of 0.533 m/s, or $Fn = 0.0642$ are considered.

The INSEAN towing tank measures 220 m in length by 9 m in breadth and is 3.8 m deep. The tests were conducted for four different water depths, see Fig. 1, using a false floor with adjustable height and dimensions of 60 m in length and 7.5 m in breadth. No special care was taken to avoid flow underneath the floor and between the floor and sidewalls of the basin.

4 CFD calculations

4.1 ReFRESCO calculations (MARIN)

ReFRESCO is a MARIN spin-off of FreSCo [12], which was developed within the VIRTUE EU Project together with Technische Universität Hamburg-Harburg (TUHH) and Hamburgische Schiffbau-Versuchanstalt (HSVA). ReFRESCO is an acronym for *Reliable and Fast Rans Equations solver for Ships, Cavitation and Offshore*. It solves the multi-phase unsteady incompressible RANS equations, complemented with turbulence models and volume-fraction transport equations for each phase. The equations are discretised using a finite-volume approach with cell-centred collocated variables. The implementation is face-based, which permits grids with elements with an

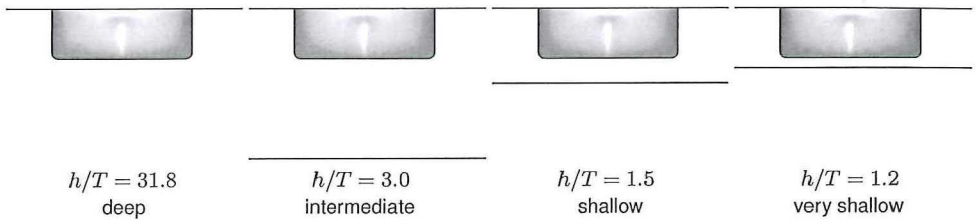

Fig. 1 Water depth h to draught T ratios considered in this study

arbitrary number of faces (hexahedrals, tetrahedrals, prisms, pyramids, etc.). The code is targeted, optimized and highly validated for hydrodynamic applications, in particular for obtaining current, wind and manoeuvring coefficients of ships, submersibles and semi-submersibles [13–16].

Several different turbulence closure models are available in REFRESCO. In this study, the Menter's 1994 version of the SST model [17] of the two-equation k–ω turbulence model is used. In the turbulence model, the Spalart correction (proposed by Dacles-Mariani et al. [18]) of the stream-wise vorticity can be activated.

For ship manoeuvres, not only oblique flow is of interest, but also the flow around the ship when it performs a rotational (yaw) motion. In RANS, the rotational motion can be modelled in several ways, such as moving the grid in a rotational motion through a stationary flow (inertial reference system), or by letting the flow rotate around the stationary ship (non-inertial reference system). For this work a non-inertial reference system is chosen. Centrifugal and Coriolis forces to account for the rotation of the coordinate system are added to the momentum equation as source terms. More information about the implementation can be found in Toxopeus [16].

4.1.1 Computational domain and grids

Multi-block structured O–O grids are used for this study for best performance of REFRESCO. Grid points have been clustered towards the hull surface and bottom to ensure proper capturing of the boundary layers. The far field boundary is generated as a cylindrical surface, to facilitate the use of a single grid for all computations. An example grid is given in Fig. 2. The diameter of the domain is 4 L_{pp}. For all cases presented in this study the y^+ values in the first cell from the wall are below 1 for the finest grid, such that the equations are integrated down to the wall.

Grids were generated with GridPro for the four different water depth h to draught T ratios, i.e., $h/T = 31.8$ representing deep water, $h/T = 3.0$ representing an intermediate water depth, $h/T = 1.5$ representing shallow water and $h/T = 1.2$ representing very shallow water, see Fig. 1. Basically, the grid topology around the hull for the four water depths was the same, the only difference being the addition of grid blocks between the bottom of the hull and the sea floor for each water depth.

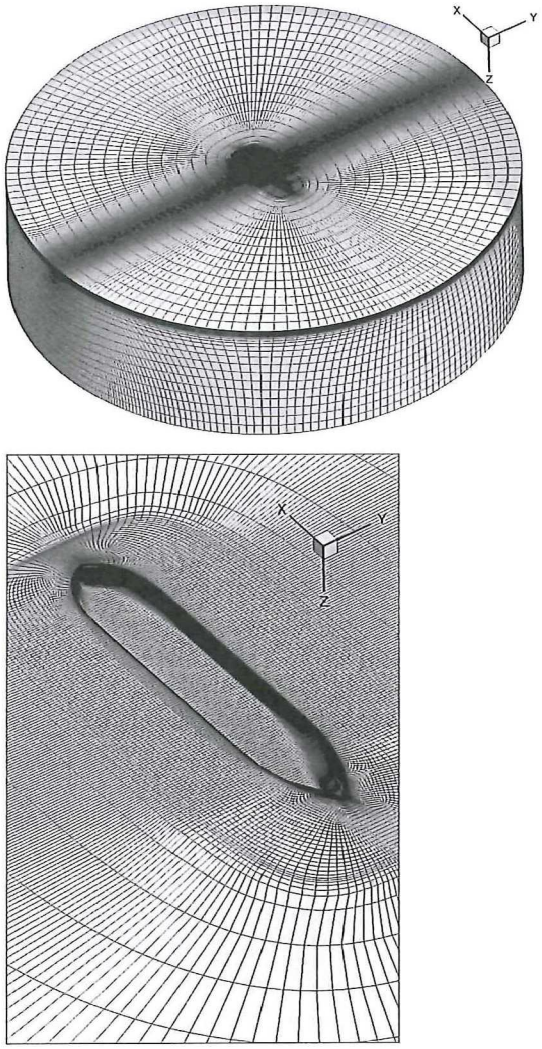

Fig. 2 Example REFRESCO grid, KVLCC2, deep water (coarsened for presentation)

Based on these grids, geometrically similar grids were generated using GridPro in order to be able to assess the discretisation errors and to accelerate the iterative procedures by using coarse grid solutions as initial flow fields for fine grid computations. Additional grids are obtained by coarsening the finest grid in all directions. Table 2 lists the grid densities used for this study.

Table 2 Grid densities used for verification and validation in REFRESCO

h/T	Grid cells (10^{-3})
31.8 (deep)	12721, 8455, 5388, 3340, 2270, 1590, 121
3.0 (intermediate)	13005, 8597, 5573, 3446, 2374, 1604, 137
1.5 (shallow)	11659, 7688, 4936, 3106, 2112, 1437, 119
1.2 (very-shallow)	11031, 7270, 4664, 2899, 1999, 1351

4.1.2 *Case setup*

The calculations presented in this study were all conducted without incorporating free-surface deformation and assuming steady flow. Based on the speeds used during the tests and the range of drift angles or yaw rates studied, the effects of Froude number and free-surface deformation on the forces on the manoeuvring ship were expected to be reasonably small and assumed to be smaller than the uncertainties due to, e.g., discretisation errors or errors in the experimental results. To simplify the calculations, symmetry boundary conditions were therefore applied on the undisturbed water surface and dynamic sinkage and trim was neglected. On the hull surface, no-slip and impermeability boundary conditions are used ($\bar{u} = 0$). For all calculations, even for deep water, the boundary condition on the bottom surface is set to moving-wall/fixed slip ($\bar{u} = \bar{V}_\infty$, with $\bar{V}_\infty$ the inflow velocity). All calculations were conducted with a Reynolds number of $Re = 3.7 \times 10^6$.

Additionally, a calculation for deep water with the finest grid was conducted with $Re = 4.6 \times 10^6$, in order to be able to compare the flow field with measurements in a wind tunnel by Lee et al. [7].

Calculations for ships at drift angles or yaw rates are conducted by setting the boundary conditions at the exterior to the proper inflow velocities. This is done using the so-called BCAUTODETECT boundary condition, which automatically applies inflow conditions ($\bar{u} = \bar{V}_\infty$) or outflow (Neumann, $\frac{\partial \phi}{\partial \bar{n}} = 0$) conditions on the cell faces, depending on the normal velocity at each cell face on the boundary. Therefore, the computational domain does not need to be changed for each new calculation and a single grid for different manoeuvring conditions can be used. Details about BCAUTODETECT can be found in Toxopeus [16].

In order to efficiently generate results for many drift angles, a routine was used to automatically increment the drift angle during a single simulation. Simulations begin with a pre-set drift angle, until a specified number of iterations is reached, or when the maximum change in the residuals is less than a specified convergence criterion. Next, the drift angle is incremented by $\Delta\beta$, by changing the inflow conditions, and the solution is continued from the solution from the previous drift angle. Starting the calculations from a converged solution at a slightly different drift angle saves time compared to performing each calculation separately from undisturbed flow. This procedure is repeated until the desired maximum inflow angle is reached. In Toxopeus [16], it is demonstrated that this approach provides the same results as those obtained with multiple single-drift angle calculations.

This procedure was designated *drift sweep* and the application has already been presented in, e.g., Toxopeus [16], Vaz et al. [14] and Bettle et al. [19].

4.2 STAR-CCM + calculations (FORCE)

The computations are performed with the Reynolds averaged Navier–Stokes (RANS) solver STAR-CCM + from CD-adapco. The code solves the RANS and continuity equations on integral form on an unstructured mesh by means of the finite volume technique. For the present calculations the temporal discretisation is based on a first order Euler difference, while spatial discretisation is performed with second order schemes for both convective and viscous terms. The pressure and the velocities are coupled by means of the SIMPLE method. Closure of the Reynolds stress problem is achieved by means of the isotropic blended k–ε/k–ω SST turbulence model with an all y^+ wall treatment, which based on the y^+ value automatically, selects the proper near wall model. The free surface is modelled with the two phase volume of fluid technique (VOF). In case squat is included in the simulation, the 6DOF module in the CFD code is applied. The heave and pitch motions are found by solving the equations of motions on each time step based on the hydrodynamic forces computed with the flow solver. The motion of the ship in the flow model is handled by mesh morphing, i.e., by stretching the computational grid locally around the ship as it moves. In the present approach the computation with squat is done in two steps. First dynamic sinkage and trim are determined with the morphing technique on a coarse grid and next the model is positioned and locked in the fine grid simulation for calculation of the hydrodynamic forces. Further details about the code can be found in the Star-CCM + User's Manual [20].

4.2.1 *Computational domain and grids*

The applied grid is an unstructured hexa-dominant polyhedral mesh, which is generated in STAR-CCM + by means of the trimmed mesh approach. The idea is to apply an orthogonal hexahedral background grid and use the shape of the ship to cut out a hole with the same geometry as the hull form. When this is done, prism layers are grown

on the geometry to resolve the boundary layer on the hull. Finally, zones with local grid refinement are used around the ship, in the gap between ship and seabed and in the free surface region. Since static drift conditions are simulated, both sides of the hull are considered instead of exploiting the centre plane symmetry. The grid near wall spacing on no-slip surfaces are in the range from $y^+ = 1$ to $y^+ = 30$.

Different grids are applied for each water depth, but in order to minimize the influence of the grid fineness when the pressure and shear forces are integrated to obtain the hydrodynamic loads, the same cell size is used on the hull surface for all grids. The location of the outer boundaries is described in the case setup section below. On the seabed, prism layers are applied to resolve the bottom boundary layer in shallow water, but not in the deep water case, where this effect is negligible. Concerning mesh size, the grids used for free surface simulations contain around 7.5 million cells, while the grids applied for simulations without free surface only contains app. 5.0 million cells, since the mesh above the still water surface can be removed. Examples on the applied grids can be seen in Fig. 3. As mentioned earlier the squat is computed an a coarse grid, which in this case consist of approximately 1 million cells. Forces are calculated with 7.5 million cells. In cases with small under keel clearance and mesh morphing there is a risk of deforming the mesh too much when the ship squats and the under keel clearance is reduced. Figure 4 shows a cross section below the ship located $0.071L$ aft of the forward perpendicular plane where the larger deformations occur due to bow down trim. As seen in the figure the deformed mesh looks fine after morphing. Further, no negative cell volumes were detected during the computation.

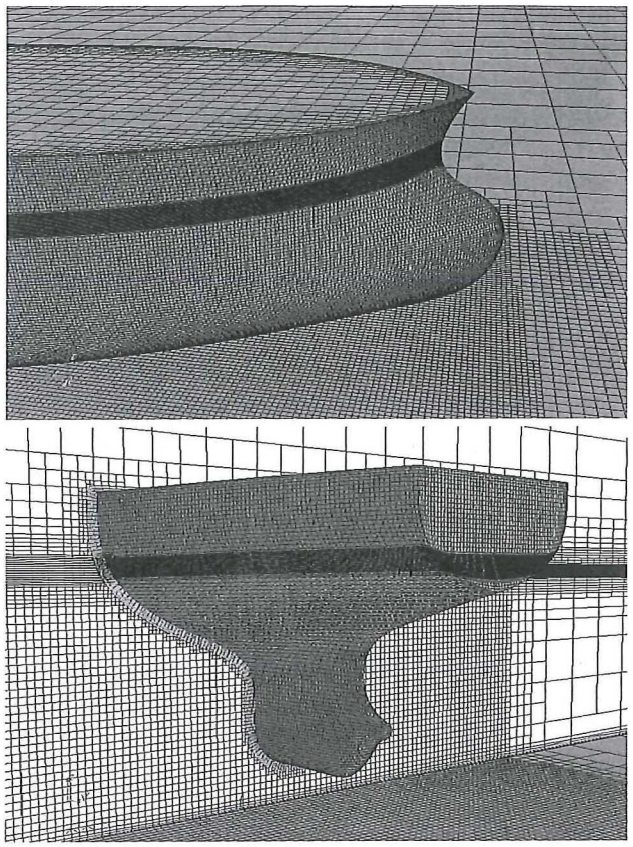

Fig. 3 Example STAR-CCM + grid applied for shallow water simulation with free surface

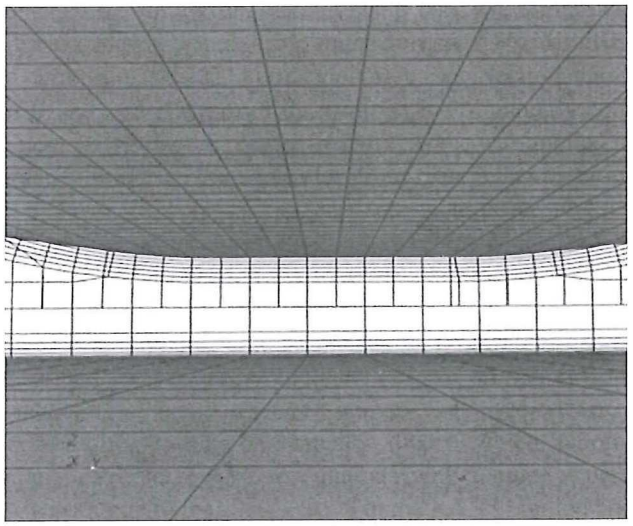

Fig. 4 Grid in gap between ship and seabed after morphing during computation of squat

4.2.2 *Case setup*

The influence of tank width, free surface effects and squat is investigated in the present computations. Except for the case where squat is included, all simulations are performed with the ship fixed at design draught and even keel. Two domain widths are considered. The narrow domain has the same width as the towing tank, where the experiments were conducted, i.e., $1.29L_{pp}$, while the wide domain has a width of $3.00L_{pp}$. For all cases the inlet boundary is located $2.36L_{pp}$ in front of the ship, while the outlet boundary is located $3.79L_{pp}$ downstream of the ship. The bottom of the domain is located according to the considered water depth. A no-slip condition is used on the hull itself. Below the ship two different boundary conditions are applied depending on the water depth. In deep water, i.e., $h/T = 8.3$, the effect of the boundary layer on the seabed is negligible, so a slip-wall condition is applied. In shallow water, i.e. $h/T = 1.5$ and 1.2, a boundary layer builds up on the seabed below the ship, which influences the flow in the gap between the bottom of the ship and the seabed. Therefore, a moving no-slip condition is applied on the seabed, so the bottom moves with the free stream speed. It should be noted that the bottom is modelled with a standard

fully turbulent boundary layer, i.e. the roughness is not adjusted to reflect the bottom in the towing tank.

For simulations without free surface the top of the domain is placed on the still water surface, where a symmetry condition is applied. On the inlet boundary the free stream speed prescribed, while the outlet boundary is modelled with a pressure condition, $p = 0$. On the sides of the domain a slip-wall boundary condition is used. When simulations with free surface and with and without squat are conducted, the domain is extended $0.65L_{pp}$ into the air above the still water level to capture the free surface deformation and a slip condition is applied as boundary condition. Further, the volume fraction is prescribed on the inlet boundary to model the still water level and the hydrostatic pressure is applied on the outlet boundary. All other boundary conditions are the same as above.

Only straight-ahead, $\beta = 0°$, and static drift, $\beta = 4°$, are simulated. In both cases the same outer domain and boundary conditions are applied and the drift angle is obtained by turning the ship 4 degrees relative to the domain and flow direction, similar to a towing tank PMM test.

4.3 ISIS-CFD calculations (ECN)

ISIS-CFD, developed by the CFD group of the Fluid Mechanics Laboratory and available as a part of the FINE^{TM}/Marine computing suite, is an incompressible unsteady Reynolds-averaged Navier–Stokes (URANS) method. The solver is based on the finite volume method to build the spatial discretisation of the transport equations. The unstructured discretisation is face-based, which means that cells with an arbitrary number of arbitrarily shaped faces are accepted. A detailed description of the solver is given in Queutey and Visonneau [21] and Duvigneau et al. [22]. The velocity field is obtained from the momentum conservation equations and the pressure field is extracted from the mass conservation constraint, or continuity equation, transformed into a pressure equation. In the case of turbulent flows, transport equations for the variables in the turbulence model are added to the discretisation. Free-surface flow is simulated with a multiphase flow approach: the water surface is captured with a conservation equation for the volume fraction of water, discretised with specific compressive discretisation schemes discussed in Queutey and Visonneau [21]. The method features sophisticated turbulence models: apart from the classical two-equation k–ω and k–ε models, the anisotropic two-equation explicit algebraic stress model (EASM), as well as Reynolds stress transport models are available, see Duvigneau et al. [22] and Deng and Visonneau [23]. The technique included for the 6 degree of freedom simulation of ship motion is described by Leroyer and Visonneau [24]. Time-integration of Newton's laws for the ship motion is combined with analytical weighted or elastic analogy grid deformation to adapt the fluid mesh to the moving ship. Furthermore, the code has the possibility to model more than two phases. For brevity, these options are not further described here.

4.3.1 Computational domain and grids

The computational domain takes into account the size of the tank, i.e., the width is 9 m and the water depth varies between 0.546 to 3.777 m. All computational domains start $2.5L_{pp}$ before the hull and extend $4L_{pp}$ after the hull. The top of the mesh for the simulation with free surface is located $0.143L_{pp}$ above the still water level. Grids were generated with Hexpress. For all test-cases, the hull is described with the same number of faces, and for the "straight-ahead" cases, the mesh contains between 1.5 and 1.7 million cells, while for the "static drift" cases, the mesh is comprised of 9.2–10 million cells. For the straight-ahead case, only one side of the ship is computed. For all cases presented in this study the y^+ values in the first cell from the wall are below 30. An example is given in Fig. 5.

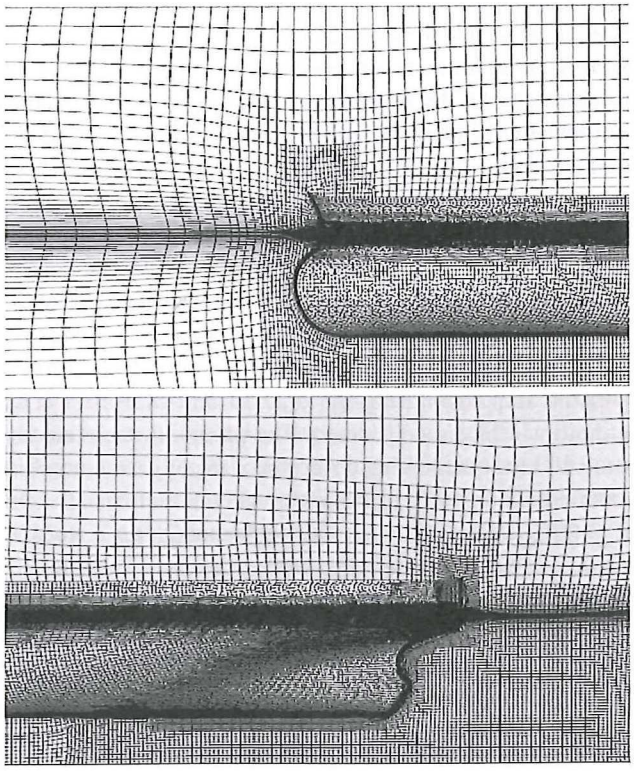

Fig. 5 Example ISIS-CFD grid, KVLCC2, shallow water configuration

4.3.2 Case setup

The calculations presented in this article were made with or without taking the free surface into account. Three water depth h to draught T ratios were studied: $h/T = 8.3$ representing deep water, $h/T = 1.5$ representing shallow water and $h/T = 1.2$ representing very shallow water and two conditions were considered: "straight-ahead", and "static drift" with a drift angle of 4°. All the computations were performed with wall function on the ship hull and free-slip on side wall and tank bottom. Since the ship is moving at model speed in the ISIS-CFD computations, the velocity at the inlet is set to zero. The turbulence model used for all test cases is the non-linear anisotropic Explicit Algebraic Stress Model (EASM). When the ship is free to sink and trim, the hull motion is computed using Newton's laws and the mesh is adapted to the movement of the ship with the analytical weighted grid deformation of ISIS-CFD, see Leroyer and Visonneau [24].

4.4 CFDShip-Iowa calculations (IIHR)

These results are a portion of those of a more comprehensive study that uses DES on a 13M grid to investigate vortical and turbulent structures for KVLCC2 tanker hull form at large drift angles with analogy to delta wings, see Xing et al. [25]. The general-purpose solver CFDShip-Iowa-V.4 (see Carrica et al. [26]) solves the unsteady RANS (URANS) or DES equations in the liquid phase of a free surface flow. The free surface is captured using a single-phase level set method and the turbulence is modelled by isotropic or anisotropic turbulence models. Numerical methods include advanced iterative solvers, second and higher order finite difference schemes with conservative formulations, parallelization based on a domain decomposition approach using the message-passing interface (MPI), and dynamic overset grids for local grid refinement and large-amplitude motions.

4.4.1 Computational domain and grids

Figure 6 shows the computational domain, grid topology, and boundary conditions. The domain extends ($-2L_{pp}$, $2L_{pp}$) in the streamwise direction (x), ($-1.5L_{pp}$, $1.5L_{pp}$) in the transverse direction (y), and ($-1.2L_{pp}$, $-0.1L_{pp}$) in the vertical direction (z). The negative z ensures that the entire ship hull is submerged in the water without solving the level set transport equation. Body-fitted "O" type grids are generated for ship hull and rectangular background grids are used for specifying boundary conditions away from the ship hull, with clustered grid near the top boundary to resolve flows around the ship. As required by the turbulence models, $y_1^+ < 1.2$ is enforced for the first grid point

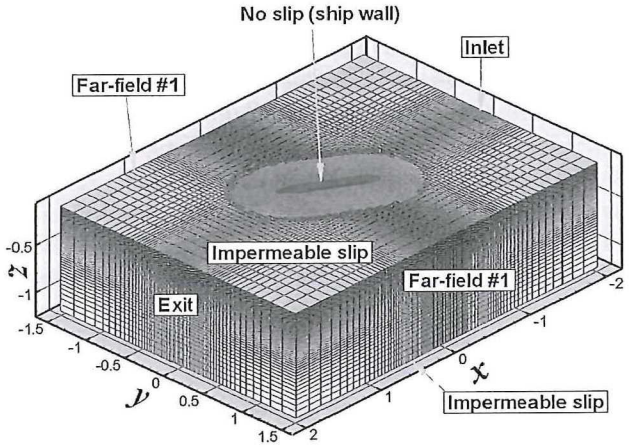

Fig. 6 CFDShip-Iowa grids, solution domain, and boundary conditions

away from the ship hull for all the grids. The grid densities for the ship hull and background are presented in Table 3 where Grids 1–4 are systematically related by a refinement ratio $\sqrt{2}$. Most of the results are presented for Grid 1, which is much finer than Grid 3 used in Xing et al. [27]. For verification studies for $\beta = 0°$, Grids 2, 3, and 4 are also used. Overall, the use of Grid 1 and DES model resolves 87 % of the total TKE in the LES region.

4.4.2 Case setup

The calculations presented in this study were all conducted without incorporating free-surface effect. The top boundary is specified as "symmetry" boundary to mimic the double-body model in the experiment. No-slip boundary conditions are used on the ship hull surface. An algebraic Reynolds stress based DES (ARS-DES) model is used. TVD2S convection scheme is used for the convection term of the momentum equation. The Reynolds number in the computations was set to $Re = 4.6 \times 10^6$.

5 Verification studies

In this article, verification and validation (V&V) of the computational results obtained with ReFRESCO and CFDShip-Iowa are conducted. Uncertainty estimates for the STAR-CCM + and ISIS-CFD solutions could not be made, due to budgetary and time constraints. Extensive procedures for V&V have been published in the past, see e.g. the ISO-GUM [28], Stern et al. [29], and recently the ASME V&V-20 standard [30]. For details regarding V&V and the nomenclature used, the readers are referred to those publications. In this article, the procedures by Eça et al. [31] and Xing and Stern [32] are used to estimate the

Table 3 Grid densities for verification and validation for CFDShip-Iowa

Grid	Ship	Background	Total	y^+
1	406 × 244 × 98 = 9,708,272	214 × 132 × 116 = 3,276,768	12,985,040	0.4
2	287 × 174 × 69 = 3,445,722	152 × 93 × 82 = 1,159,152	4,604,874	0.6
3	203 × 122 × 49 = 1,213,534	107 × 66 × 58 = 409,596	1,623,130	0.8
4	144 × 88 × 35 = 443,520	76 × 47 × 41 = 146,452	589,972	1.1

discretisation uncertainty. Summarising, the simulation numerical uncertainty U_{SN} is obtained from.

$$U_{SN}^2 = U_I^2 + U_G^2 + U_T^2$$

where U_I, U_G and U_T are the uncertainties due to the iterative procedure, the discretisation in space and the discretisation in time, respectively.

The purpose of validation is to assess the interval of the modelling uncertainty and thereby ascertain the usefulness of the modelling approach. The comparison error E is defined by the difference between the simulation S and data D values. Note that for the comparison error E, two definitions can be found in literature: $E = S - D$, as in e.g. the ASME standard, or $E = D - S$, as proposed in e.g. Coleman and Stern [33]. In the present work, $E = S - D$ is used to indicate the comparison error.

The validation uncertainty U_{val} is defined as:

$$U_{val} = \sqrt{U_{SN}^2 + U_D^2 + U_{input}^2}$$

The uncertainty due to errors in the simulation input parameters U_{input} is not considered in this article and therefore assumed to be zero. If $|E| < U_{val}$, the combination of all the errors in S and D is smaller than the validation uncertainty and validation is said to be achieved at the U_{val} interval.

5.1 Iterative convergence

5.1.1 ReFRESCO

All calculations were run until the maximum normalized residual res_{max} (the so-called L_∞ norm) between successive iterations had dropped well below 1×10^{-5} or when further iterative convergence was not obtained. The changes in the non-dimensional integral quantities (forces and moments) were well below 1×10^{-7}, which is several orders smaller than the uncertainty due to discretisation in space. Therefore, the uncertainty due to the iterative process is negligible compared to other uncertainties: $U_I = 0$.

5.1.2 CFDShip-Iowa

All simulations used the "unsteady" mode of the code. The tolerances for solution of the momentum equation and the pressure equation are 1×10^{-5} and 1×10^{-6}, respectively. Parametric studies on the nonlinear iterations for each time step ensure iterative convergence at each time step. Results show that by increasing the nonlinear iterations from 4 to 5 for each time step, the difference for the resistance $X = X_f + X_p$ is less than 0.5 %. Simulations used five nonlinear iterations. The simulation is then advanced to the next time step. Iterative uncertainties U_I are estimated by computing the deviation of the variable from its mean value based on the range of the maximum and minimum values of the last period of the oscillation where the variable is the resistance and the running mean of the resistance for steady and unsteady flows, respectively.

Statistical convergence of running mean on the time history of the resistance establishes statistically stationary unsteady solutions. The criterion for statistical convergence of the resistance is that $U_I < 0.4\ \%S_{mean}$, which is ensured for all cases run in this study. Based on this criterion, X converges after 3.2 flow times for ARS-DES. An additional 2.5 flow times after convergence was calculated in order to perform the statistical analysis for the mean, dominant frequency, and all the turbulence analysis.

5.2 Discretisation error in time and space

5.2.1 ReFRESCO

Using the procedure proposed by Eça et al. [31], the uncertainties in the forces and moments are estimated. Based on an analysis of the results for each grid, it was decided to use the 5 finest grids for the uncertainty analysis. The number of grids n_g used depended on the scatter in the results for the coarsest grids. It was found that for grids with a relative step size h_i of 2 and above ($h_i = \sqrt[3]{N_1/N_i}$ with N_i the number of cells in grid i), the results are not consistent with the finer grid results. This means that with the present grid layout,[1] grids of more than

[1] In other studies in which the k-ω SST turbulence model was used, we have found that for grids with more excessive clustering of cells towards the wall, resulting in y^+ values considerably lower than 1, the uncertainty estimates become much more consistent and closer to the expected order of convergence. This is mainly due to the fact that ω tends to infinity at the wall and therefore cells should be placed close to the wall in order to capture the large gradients in ω.

about 1.6×10^6 cells are required to obtain a reliable solution of the forces and moments. Table 4 presents the estimated discretisation uncertainties for $\beta = 0°$ in deep, shallow and very shallow water. In this table, S indicates the value of the solution on the finest grid, U_S the uncertainty in the solution and p the observed order of convergence. In Tables 5 and 6 the uncertainties for $\beta = 4°$ and $\gamma = 0.4$ are shown.

In deep water, monotonic convergence for X is not found for $\beta = 0°$ and $\beta = 4°$. In that case, the data range is used to estimate the uncertainty, combined with a factor of safety of 3. Due to the small difference of X on the different grids, the estimated uncertainty is however small, i.e., $U_X = 1.3$ %S. For X_p and apparent order of convergence much larger than the theoretical order of 2 is found. This indicates irregular behaviour of the solution upon grid refinement and therefore a factor of safety of 3 is adopted as well.

For the shallow water depth cases of $h/T = 1.5$ and $h/T = 1.2$, larger uncertainties are found, up to $U_X = 11.8$ %S, which is mainly caused by slow convergence ($p < 1$) The cases with yaw rates show the largest uncertainties, also due to slow convergence and still large changes between the solutions on the different grids.

Convergence is found for the Y force for all conditions. Interestingly, for $\beta = 4°$ the U_Y in %S appears to reduce with reducing water depth, see also Figs. 7 and 8. In absolute values, however, the uncertainty remains about the same. For the case with yaw rate, $\gamma = 0.4$, the uncertainties are large and increase with decreasing water depth, as shown in Fig. 21. During yaw motion, the forces on the bow and stern are large but of opposite sign, which results in a relatively small total Y force and subsequently leads to large uncertainties.

Table 4 Uncertainty estimate, REFRESCO, $\beta = 0°$

Item	S	U_S (%)	p
Deep water			
X_p	-3.06×10^{-3}	12.8	3.45
X_f	-1.49×10^{-2}	10.4	0.25
X	-1.80×10^{-2}	1.3	[a]
Shallow water $h/T = 1.5$			
X_p	-5.77×10^{-3}	4.3	[b]
X_f	-1.66×10^{-2}	3.1	1.38
X	-2.24×10^{-2}	7.0	0.63
Very shallow water $h/T = 1.2$			
X_p	-8.15×10^{-3}	3.4	[b]
X_f	-1.73×10^{-2}	4.5	0.96
X	-2.55×10^{-2}	11.8	0.23

[a] Oscillatory convergence

[b] Monotonic divergence

Table 5 Uncertainty estimate, REFRESCO, $\beta = 4°$

Item	S	U_S (%)	p
Deep water			
X	-1.83×10^{-2}	1.3	[a]
Y	1.53×10^{-2}	15.7	0.92
N	1.02×10^{-2}	7.2	[b]
Shallow water $h/T = 1.5$			
X	-2.31×10^{-2}	10.9	0.40
Y	3.41×10^{-2}	6.8	2.46
N	2.23×10^{-2}	2.5	0.80
Very shallow water $h/T = 1.2$			
X	-2.57×10^{-2}	9.0	[c]
Y	7.89×10^{-2}	5.4	1.29
N	3.46×10^{-2}	1.2	1.24

[a] Oscillatory convergence

[b] Monotonic divergence

[c] Oscillatory divergence

Table 6 Uncertainty estimate, REFRESCO, $\gamma = 0.4$

Item	S	U_S (%)	p
Deep water			
X	-1.57×10^{-2}	12.4	1.21
Y	1.58×10^{-2}	16.9	1.82
N	-1.77×10^{-2}	7.3	1.43
Shallow water $h/T = 1.5$			
X	-2.09×10^{-2}	51.8	0.50
Y	2.30×10^{-2}	98.3	0.66
N	-2.15×10^{-2}	24.1	0.88
Very shallow water $h/T = 1.2$			
X	-2.53×10^{-2}	99.7	0.26
Y	4.89×10^{-2}	237.7	0.24
N	-2.89×10^{-2}	13.1	1.36

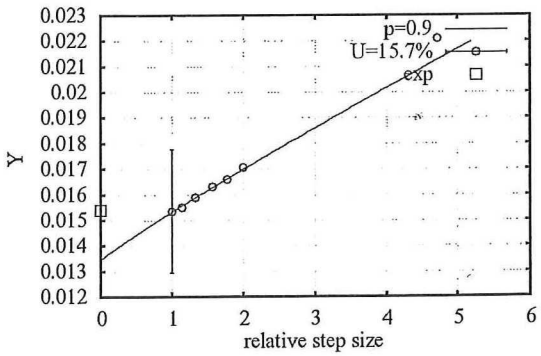

Fig. 7 Uncertainty estimate, REFRESCO, Y force, $\beta = 4°$, deep water

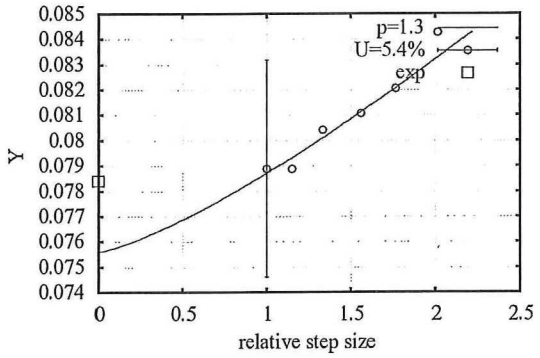

Fig. 8 Uncertainty estimate, ReFRESCO, Y force, $\beta = 4°$, very shallow water

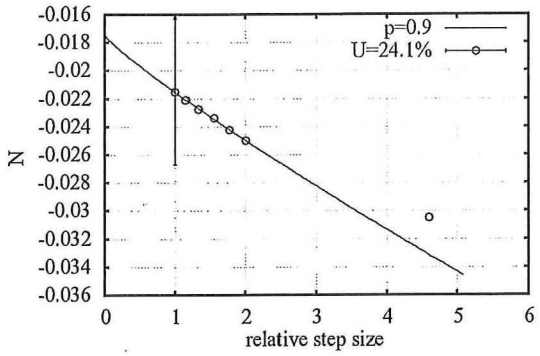

Fig. 9 Uncertainty estimate, ReFRESCO, N moment, $\gamma = 0.4$, shallow water

The uncertainties in the N moment are found to be more reasonable than the uncertainties in X or Y, see Figs. 9 and 10. This is probably caused by the fact that during pure yaw motion, the yaw moment (sum of contributions) is better defined than the longitudinal force or side force (difference between contributions). However, for $\gamma = 0.4$, the uncertainty is judged to be too high. Especially for shallow water with $h/T = 1.5$, the uncertainty is high, due to a low apparent order of convergence and large grid dependency, see Fig. 9.

The theoretical order of convergence should be 2 for ReFRESCO. However, due to flux limiters, discretisation of the boundary conditions and other factors, the apparent order of convergence is expected to be between 1 and 2 for geometrically similar grids in the asymptotic range. Considering uncertainty estimates for the various water depths and conditions, the apparent orders do not always follow this expectation. This indicates that either even finer grids are required, or that scatter in the results spoils the uncertainty estimate.

5.2.2 *CFDShip-Iowa*

Quantitative verification is conducted for the grids following the factor of safety method, see Xing and Stern [32]. The design of the grids enables two grid-triplet studies with grid refinement ratio $r = \sqrt{2}$ (1, 2, 3 and 2, 3, 4). Larger r is not used since the coarse grids will be too coarse such that different flow physics are predicted on different grids as shown by the use of $r = \sqrt{2}$ at $\beta = 0°$, i.e., steady vs. unsteady. The use of finer grids than Grid 1 may help as shown by the monotonic convergence for 5415 test case with grids up to 276 M (see Bhushan et al. [34]), but simulations are too expensive and beyond the scope of the current study. Smaller r is not used either since solution changes will be small and the sensitivity to grid-spacing may be difficult to identify compared with iterative errors. Quantitative evaluation for time-step was not possible since large time-step leads to unstable solutions for ARS-DES on Grid 1 and simulations using smaller time-step are too expensive. Nonetheless, the current time-step ($dt = 0.002$) is only 20 % of the typical dt for CFD simulations in ship hydrodynamics and it is sufficiently small to resolve all the unsteadiness of the vortical structures and turbulent structures.

Table 7 Verification for CFDShip-Iowa, ARS-DES

Variables	Grids	R_G	P_G	U_G	δ/E	U_V	U_D
X	2, 3, 4	0.125	3.00	1.716	2.1	3.70	3.3
X_f	1, 2, 3	0.059	4.09	0.228	1.4	–	–
X_f	2, 3, 4	0.447	1.16	4.07	1.3	–	–
X_p	1, 2, 3	−1.1	Oscillatory divergence			–	–
X_p	2, 3, 4	−1.1	Oscillatory divergence			–	–

U_G is $\%S_{fine}$, δ is $\%X_{f,ITTC}$ for X_f, E, U_V, and U_D is $\%D$

Previous simulation using ARS-DES on Grid 3 showed that flow at $\beta = 0°$ for KVLCC2 is steady and thus BKW or ARS model was used (Xing et al. [27]). On Grid 1, ARS shows steady flow, whereas ARS-DES predicts unsteady flow. Table 7 shows V&V for the resistance. The experimental data used to obtain the comparison errors is presented in Table 11. For $\beta = 0°$, monotonic convergence is only achieved on (2, 3, 4) for X and on (2, 3, 4) and (1, 2, 3) for X_f. The estimated orders of accuracy show large oscillations as P_G has values from 1.16 to 4.09. X_p shows oscillatory divergence on the two grid triplets.

Overall the solutions are not in the asymptotic range, which was attributed to several causes. At $\beta = 0°$, ARS-DES on Grid 1 shows unsteady flow, whereas all other grids predict steady flows and thus they are resolving different flow physics. Further refinement of the grids may help but subject to the problem of separating iterative errors and grid solution changes on fine grids. Furthermore, grid refinement for DES changes the numerical errors and the sub-grid scaling modelling errors simultaneously, which was not considered for all available solution

verification methods. It should be also noted that all grid-triplet studies except X_f for (2, 3, 4) estimate $P_G > 2$, which cause unreasonably small uncertainties due to a small error estimate. Recently, an alternative form of the FS method (FS_1 method) was developed and evaluated using the same dataset as the FS method but using p_{th} instead of p_{RE} in the error estimate for $P_G > 1$ (Xing and Stern [35]). The FS_1 and FS methods are the same for $P_G < 1$. For $p_{th} = 2$ and grid refinement ratio $r = 2$, the FS_1 method is less and more conservative than the FS method for $1 < P_G \leq 1.235$ and $P_G > 1.235$, respectively. As a result, the FS_1 method may have an advantage for uncertainty estimates when $P_G > 2$ where the FS and other verification methods likely predict unreasonably small uncertainties due to small error estimate. The use of FS_1 method will increase U_G from 1.716 $\%S_{fine}$ to 19.485 $\%S_{fine}$ and thus U_V from 3.70 $\%D$ to 19.4 $\%D$. However, since the dataset to derive/validate the FS and FS_1 methods is restricted to $P_G < 2$, the pros/cons of using the FS or FS_1 method cannot be validated.

6 Validation

In this section, the CFD results will be compared to the available measurements. First, flow features will be qualitatively compared to wind tunnel test results presented by Lee et al. [7]. Second, the predicted forces and moments will be validated using the measurements conducted by INSEAN. Additionally, the results obtained at the higher Reynolds number ($Re = 4.6 \times 10^6$) will be validated. The validation will mostly focus on the ReFRESCO and CFDShip-Iowa results, since for these solutions uncertainty estimates are available. A more general comparison between the results from the different solvers is given in Sect. 6.

6.1 Flow features

Figure 11 shows the comparison of the experimental data and CFD for the averaged axial velocity at the propeller plane. The experiment clearly shows hook-shape pattern of the axial velocity. As explained by Larsson et al. [36] in the CFD Workshop Gothenburg 2010, this pattern was caused by an intense stern bilge vortex and a secondary counter-rotating vortex close to the vertical plane of symmetry. The secondary vortex cannot be seen clearly in the experiment due to limitation of the resolution. CFDShip-Iowa ARS on grid 1 under-estimates the size of the main vortex and predicts steady flow. CFDShip-Iowa ARS-DES on grid 1 shows significant improvements on estimating the size of the main vortex and prediction of the hook-shape pattern. The ReFRESCO result contains the stern bilge vortex and counter-rotating secondary vortex, but the hook shape is not well resolved. In Toxopeus [37], it was shown that by activating the Spalart correction of the stream-wise vorticity the hook shape could be resolved, indicating the sensitivity of the results to the turbulence model.

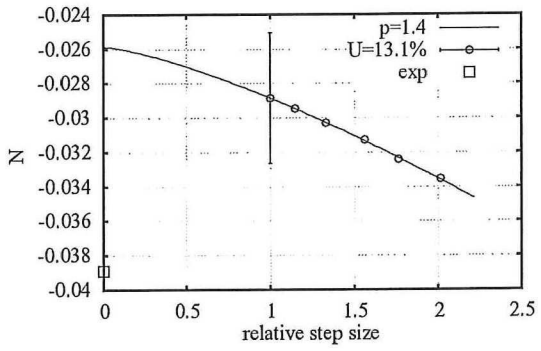

Fig. 10 Uncertainty estimate, ReFRESCO, N moment, $\gamma = 0.4$, very shallow water

Figure 12 shows the total turbulent kinetic energy k, which shows the similar trend as that for axial velocity distributions shown in Fig. 11, but with the peak value of k ($\sim 2.1\ \%U_0^2$) over-predicted by 35 % in the CFDShip-Iowa result. In the ReFRESCO results, the hook-shape is less developed and only one peak is clearly visible, but the peak value is quite close to the measurements (3.5 % underprediction).

6.2 Forces and moments

Tables 8, 9, 10 present the EFD and CFD results for the different water depths and manoeuvring conditions. The comparison errors E, numerical and data uncertainties U_{SN} and U_D and the validation uncertainties U_{val} are given if available. For $\beta = 0°$, U_D is assumed to be the same as for $\beta = 4°$. For $\gamma = 0.4$, U_D is estimated based on repeat tests, or taken from the $\beta = 4°$ condition. This is done to have at least the possibility to obtain U_{val}, although it is questionable whether single observations have the same uncertainties as the average value from multiple runs (for which outliers in the data are less significant). Note: after careful analysis of the results for $\gamma = 0.4$ in shallow water, it was found that the transverse force Y obtained from the EFD could not be used for validation of the CFD results for these conditions.

6.2.1 Straight ahead sailing

For $\beta = 0°$ in deep water, see Table 8, uncertainties are available for the ReFRESCO and CFDShip-Iowa results. In both cases validation of the solution is obtained ($|E| < U_{val}$), at levels of 6.5 $\%D$ and 6.6 $\%D$ respectively. The comparison errors for all computations are reasonably small, i.e., 4.6 $\%D$ or less.

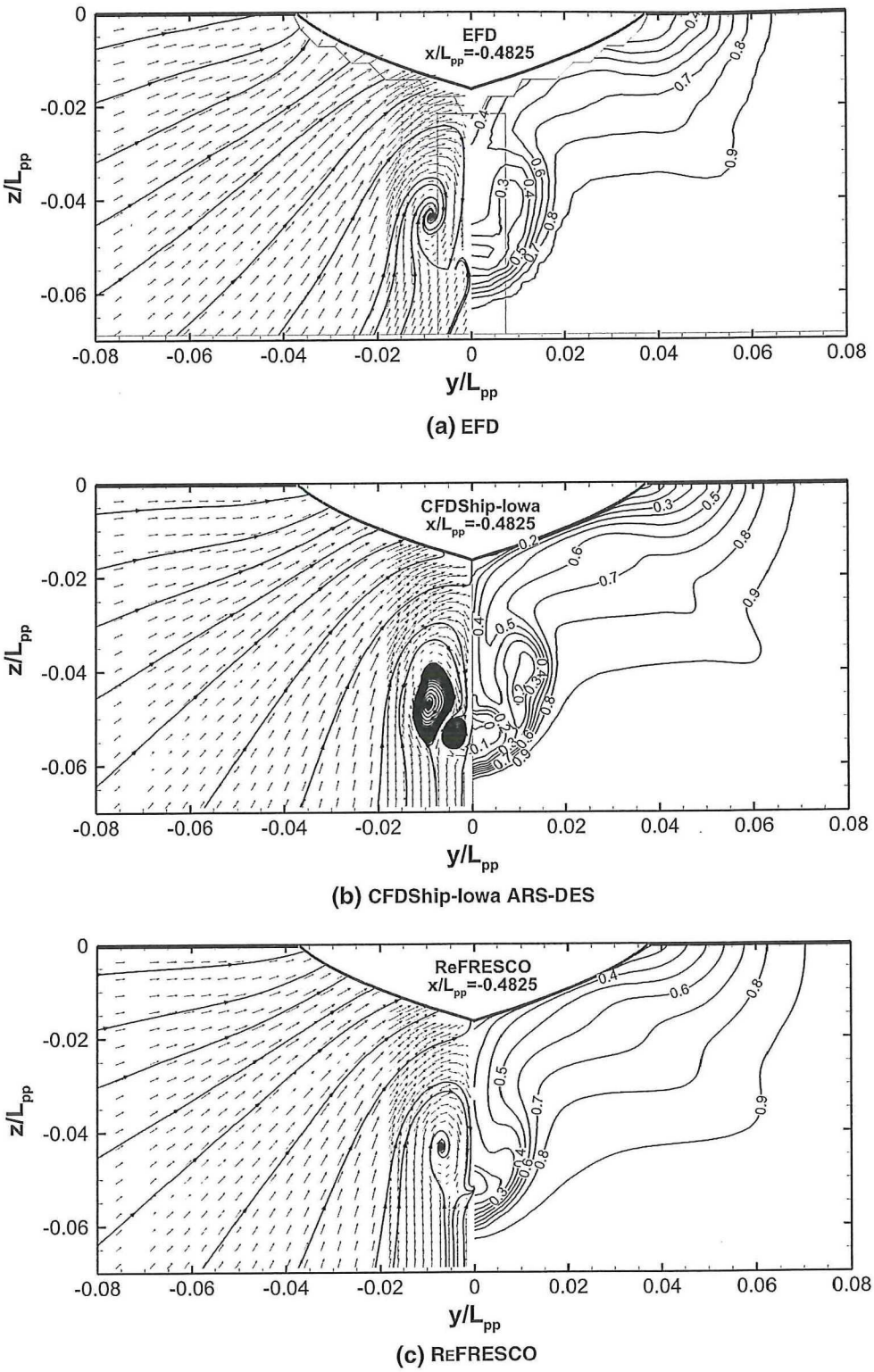

Fig. 11 Transverse (*left panel*) and axial wake (*right panel*), $Re = 4.6 \times 10^6$, deep water, $\beta = 0°$, $x/L_{pp} = -0.4825$

For the shallow water cases with $\beta = 0$ validation is not obtained for the REFRESCO results. This means that modelling errors are present in the results. The modelling errors are likely to be caused by the absence of the basin walls, and neglect of sinkage, trim and free surface deformation. For $h/T = 1.5$, all CFD results show negative comparison errors (under-prediction of the resistance), while for $h/T = 1.2$ most predictions with modelling of the basin walls over-predict the resistance. Although uncertainties are not available and conclusions are therefore

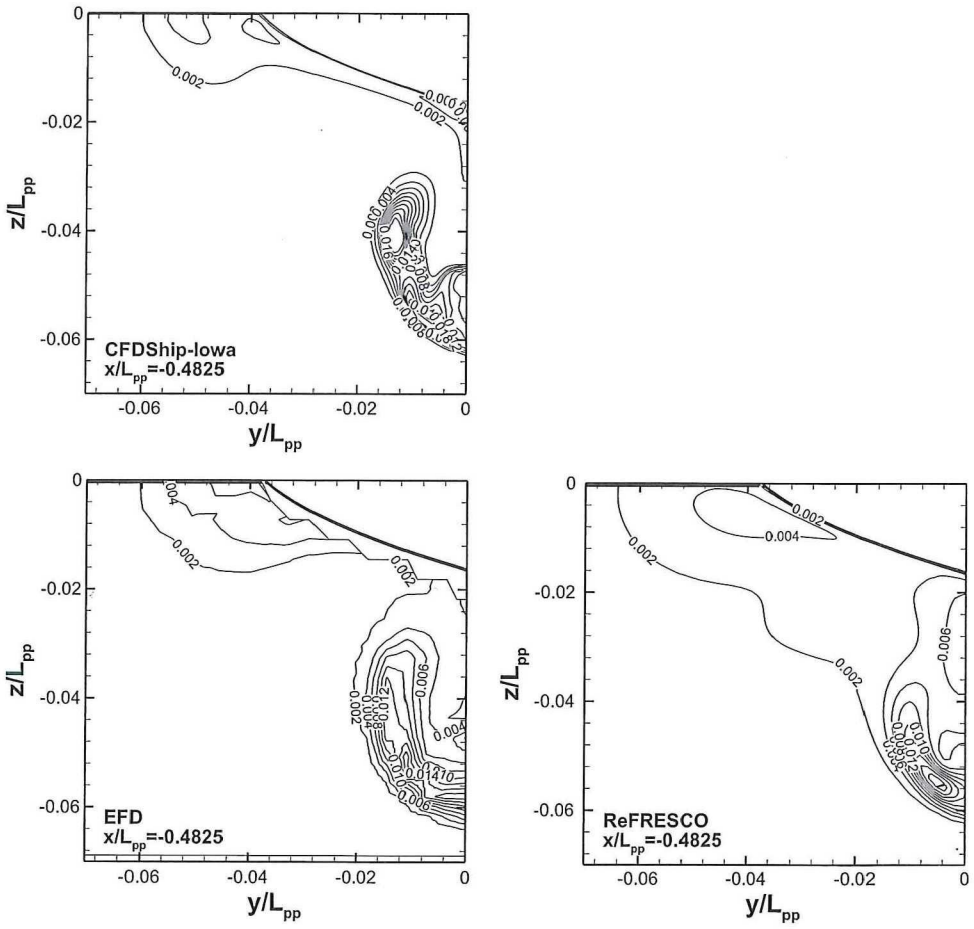

Fig. 12 Turbulent kinetic energy contours, $Re = 4.6 \times 10^6$, deep water, $\beta = 0°$, $x/L_{pp} = -0.4825$

difficult to draw, this might be caused by the existence of a gap between the false bottom and the basin walls during the experiments. Such a gap will effectively reduce the blockage in the basin, which will be most pronounced in the most extreme shallow water conditions.

As expected, all $\beta = 0°$ results indicate that modelling the basin walls will increase the resistance compared to using a wide domain (about 10 %D, see also below). The ISIS-CFD results show that modelling the free surface will increase the resistance further, i.e. by about 3 %D in deep water, 5 %D for $h/T = 1.5$ and 9 %D for $h/T = 1.2$. An additional increase is found when the dynamic trim and sinkage is considered as well: about 1 %D.

6.2.2 *Sailing at a drift angle*

For a drift angle of $\beta = 4°$, the largest number of results are available. Uncertainties are available for the ReFRESCO results, and validation for Y is obtained for deep water at a level of 18.1 %D, see Table 9. Validation for X and N is not obtained ($|E| > U_{val}$), indicating modelling errors. Considering all CFD results, the scatter in Y and N is judged to be small, i.e., $\sigma_S = 3$ %S, and much smaller than the comparison error. All CFD results consistently over-predict the X force and under-predict both the Y force and the N moment. For deep water, the influence of modelling the basin walls on the results is judged to be negligible. There seems to be a slight influence of modelling free surface deformation on the resistance, but without uncertainty estimates, the difference cannot be validated.

For a shallow water depth of $h/T = 1.5$, no validation is achieved, although $|E_N|$ is close to U_{val} for N. Based on the different results, it is expected that the modelling error is mainly caused by the neglect of the basin walls. Judging from the trends in the Star-CCM + results, using a tank domain instead of a wide domain will on average increase the resistance, the Y force and N moment by about 8, 8 and 7 %D, respectively. Modelling free surface will increase the resistance and Y force by about 5 and 4 %D.

In very shallow water, validation is achieved for Y and N, at levels of 5.3 and 8.1 %D respectively. For X, a modelling error is present, which is probably caused by the neglect of the basin walls, free surface deformation and sinkage and trim. On average, using a tank domain instead of a wide domain will increase the resistance, the Y force

Table 8 Validation, $\beta = 0°$

Result	FS	Domain	Sinkage (m)	Trim (°)	X'	E %D	U_{SN} %S	U_{val} %D
Deep water, $U_D = 6.4$ %D								
EFD	Yes	Tank	0	0	−0.0179	–	–	–
REFRESCO	No	Wide	0	0	−0.0180	0.3	1.3	6.5
Star-CCM+	No	Tank	0	0	−0.0188	4.6	–	–
ISIS-CFD	No	Tank	0	0	−0.0178	−0.8	–	–
ISIS-CFD	Yes	Tank	0	0	−0.0183	2.0	–	–
ISIS-CFD	Yes	Tank	0.0016	−0.0163	−0.0184	2.6	–	–
CFDShip-Iowa[a]	No	Wide	0	0	−0.0180	0.6	1.7	6.6
Shallow water, $h/T = 1.5$, $U_D = 11.3$ %D								
EFD	Yes	Tank	0	0	−0.0286	–	–	–
REFRESCO	No	Wide	0	0	−0.0224	−21.8	7.0	12.6
Star-CCM+	No	Tank	0	0	−0.0251	−12.3	–	–
ISIS-CFD	No	Tank	0	0	−0.0247	−13.8	–	–
ISIS-CFD	Yes	Tank	0	0	−0.0260	−9.2	–	–
ISIS-CFD	Yes	Tank	0.0048	−0.0291	−0.0262	−8.5	–	–
Very shallow water, $h/T = 1.2$, $U_D = 4.6$ %D								
EFD	Yes	Tank	0	0	−0.0310	–	–	–
REFRESCO	No	Wide	0	0	−0.0255	−17.7	11.8	10.8
Star-CCM+	No	Tank	0	0	−0.0336	8.5	–	–
ISIS-CFD	No	Tank	0	0	−0.0292	−5.7	–	–
ISIS-CFD	Yes	Tank	0	0	−0.0321	3.6	–	–
ISIS-CFD	Yes	Tank	0.0066	−0.0515	−0.0324	4.6	–	–

[a] These results have been corrected for the difference in Reynolds number by: $X'(Re = 3.7 \times 10^6) = X'(Re = 4.6 \times 10^6) \times C_{F,ITTC}(Re = 4.6 \times 10^6)/C_{F,ITTC}(Re = 3.7 \times 10^6)$

and N moment by about 12, 12 and 10 %D respectively, based on the trends in the Star-CCM + solutions. Also for this water depth the resistance and Y force will increase by about 5 and 4 %D when modelling free surface. Noteworthy is the fact that validation is achieved for Y in deep water and very shallow water, but not for a water depth of $h/T = 1.5$. This may indicate opposing trends due to the proximity of the basin walls and the existence of gaps between the false floor and the basin walls during the experiments.

The influence of modelling trim and sinkage as found in the Star-CCM + results appears to be very large: 8 %D in Y and 17 %D in N. Unfortunately, uncertainty values are not available and therefore it is hard to judge whether this is caused by the modelling or due to uncertainties in discretisation or iterative convergence.

6.2.3 Sailing with yaw rate

Only REFRESCO results are available for the ship sailing with a yaw rate. In this section, only results for $\gamma = 0.4$ are considered. For validation, the mean X and first harmonic damping components Y and N of the EFD oscillatory yaw tests performed by INSEAN are used. For deep water, validation is obtained for X at a level of 13.4 %D. Modelling errors appear to be present in Y and N, which may be caused by the neglect of free surface, as indicated for the drift condition. For $h/T = 1.5$, validation is obtained for N at a level of 20 %D, and for $h/T = 1.2$ X is validated at a level of 98 %D. All these levels are judged to be large and are mainly caused by the large uncertainties in the numerical results.

6.2.4 Validation for $Re = 4.6 \times 10^6$

For the KVLCC2, a resistance test was conducted by Kim et al. [8] and the results of this test were used for the CFD Workshop Gothenburg 2010 [5]. However, this test was conducted with the rudder attached to the model, which makes a direct comparison with our results impossible.

The KVLCC2M is a variant of the KVLCC2 in which the lines were slightly faired compared to the original KVLCC2 hull form. The difference between the two hull forms is very small and therefore differences in the resistance are expected to be small as well. Captive tests with the bare hull KVLCC2M were conducted by Kume et al.

Table 9 Validation, $\beta = 4°$

Result	FS	Domain	Sinkage	Trim	D; S			E %D			U_D %D; U_{SN} %S			U_{val} %D		
			(m)	(deg)	X'	Y'	N'	X'	Y'	N'	X'	Y'	N'	X'	Y'	N'
Deep water																
EFD	Yes	Tank	0	0	−0.0162	0.0159	0.0116	–	–	–	5.5	9.9	6.0	–	–	–
ReFRESCO	No	Wide	0	0	−0.0183	0.0153	0.0102	12.8	−3.7	−12.4	1.3	15.7	7.2	5.7	18.1	8.7
Star-CCM+	No	Wide	0	0	−0.0175	0.0144	0.0106	7.7	−9.6	−9.1	–	–	–	–	–	–
Star-CCM+	Yes	Wide	0	0	−0.0185	0.0149	0.0106	14.2	−6.2	−8.7	–	–	–	–	–	–
Star-CCM+	No	Tank	0	0	−0.0177	0.0146	0.0107	9.2	−8.3	−8.0	–	–	–	–	–	–
Star-CCM+	Yes	Tank	0	0	−0.0188	0.0153	0.0106	16.0	−3.5	−8.6	–	–	–	–	–	–
ISIS-CFD	Yes	Tank	0	0	−0.0197	0.0154	0.0100	21.4	−3.1	−14.2	–	–	–	–	–	–
Shallow water, $h/T = 1.5$																
EFD	Yes	Tank	0	0	−0.0281	0.0380	0.0234	–	–	–	11.3	2.8	3.6	–	–	–
ReFRESCO	No	Wide	0	0	−0.0231	0.0341	0.0223	−17.8	−10.3	−4.5	10.9	6.8	2.5	14.5	6.7	4.4
Star-CCM+	No	Wide	0	0	−0.0220	0.0334	0.0223	−21.8	−12.3	−4.4	–	–	–	–	–	–
Star-CCM+	Yes	Wide	0	0	−0.0234	0.0351	0.0223	−16.9	−7.6	−4.5	–	–	–	–	–	–
Star-CCM+	No	Tank	0	0	−0.0240	0.0367	0.0239	−14.5	−3.6	2.1	–	–	–	–	–	–
Star-CCM+	Yes	Tank	0	0	−0.0256	0.0381	0.0240	−8.7	0.1	2.7	–	–	–	–	–	–
ISIS-CFD	Yes	Tank	0	0	−0.0282	0.0383	0.0234	0.4	0.7	0.2	–	–	–	–	–	–
Very shallow water, $h/T = 1.2$																
EFD	Yes	Tank	0	0	−0.0332	0.0812	0.0323	–	–	–	4.6	1.0	8.0	–	–	–
ReFRESCO	No	Wide	0	0	−0.0257	0.0789	0.0346	−22.6	−2.8	7.2	9.0	5.4	1.2	8.4	5.3	8.1
Star-CCM+	No	Wide	0	0	−0.0258	0.0855	0.0347	−22.4	5.3	7.6	–	–	–	–	–	–
Star-CCM+	Yes	Wide	0	0	−0.0268	0.0916	0.0344	−19.2	12.9	6.5	–	–	–	–	–	–
Star-CCM+	No	Tank	0	0	−0.0291	0.0974	0.0373	−12.4	20.0	15.5	–	–	–	–	–	–
Star-CCM+	Yes	Tank	0	0	−0.0314	0.0989	0.0384	−5.5	21.9	18.9	–	–	–	–	–	–
Star-CCM+	Yes	Tank	0.009	−0.047	−0.0311	0.1051	0.0439	−6.4	29.5	36.0	–	–	–	–	–	–
ISIS-CFD	Yes	Tank	0	0	−0.0381	0.1017	0.0360	14.8	25.3	11.5	–	–	–	–	–	–

[38]. These results were used for the CFD Workshop Tokyo 2005 [39]. Unfortunately, these tests were conducted at a slightly different Reynolds number of $Re = 3.945 \times 10^6$. In order to validate our predictions, estimations of the KVLCC2 bare hull resistance have been made based on these measurements, see the Appendix at the end of this article.

In Table 11, the estimated EFD and CFD values are given, together with the comparison errors. For CFDShip-Iowa ARS-DES at $\beta = 0°$, validation for X is achieved on grids (2,3,4) at a level of 3.7 %D, since $|E| < U_V$ (Table 7). Although the solutions are not in the asymptotic range, E between the running mean and experimental data are less than 3 %D. Table 11 also compares the predicted frictional resistance X_f with ITTC 1957 and the total resistance X with the experimental data on different grids. As the grids are refined from 4 to 1, δ changes from more −1.9 %ITTC to 1.4 %ITTC for X_f and E changes from −1.1 to 2.9 %D for X. By excluding Grid 4, the averaged δ and E are 1 %ITTC and 2.3 %D for X_f and X, respectively.

Assuming $U_{SN} = 1.3$ %S (see Table 4) for the ReFRESCO solution, a validation uncertainty of $U_{val} = 3.6$ %D is obtained and therefore validation is achieved.

7 Discussion of the results

7.1 Comparison of flow fields

In Figs. 13, 14, 15, 16, 17, 18, 19, wake fields are presented to study the differences between the various results. In Fig. 13, three different solutions are given for deep water and $\beta = 0°$. Qualitatively, the results are very similar, although the strength of the bilge vortex appears to be slightly different between the results. Considering the prediction of the hook-shape and the secondary vortex, the ISIS-CFD results have the best resemblance with the measurements, see also Fig. 11. This is probably caused by the use of a more advanced turbulence model.

The different wake fields predicted by ISIS-CFD for deep water and $\beta = 0°$ are shown in Fig. 14. The influence of modelling the free surface or incorporating trim and sinkage on the local wake field is very small and probably

Table 10 Validation, $\gamma = 0.4$

Result	FS	Domain	Sinkage	Trim	D; S			E %D			U_D %D; U_{SN} %S			U_{val} %D		
			(m)	(°)	X'	Y'	N'	X'	Y'	N'	X'	Y'	N'	X'	Y'	N'
Deep water																
EFD	Yes	Tank	0	0	−0.0156	0.0193	−0.0159	–	–	–	4.9	2.8	1.9	–	–	–
ReFRESCO	No	Wide	0	0	−0.0157	0.0158	−0.0177	1.0	−18.3	11.6	12.4	16.9	7.3	13.4	14.1	8.4
Shallow water, $h/T = 1.5$																
EFD	Yes	Tank	0	0	−0.0264	–	−0.0264	–	–	–	11.3	–	3.6	–	–	–
ReFRESCO	No	Wide	0	0	−0.0209	0.0230	−0.0215	−21.0	–	−18.5	51.8	98.3	24.1	42.5	–	20.0
Very shallow water, $h/T = 1.2$																
EFD	Yes	Tank	0	0	−0.0258	–	−0.0389	–	–	–	4.6	–	8.0	–	–	–
ReFRESCO	No	Wide	0	0	−0.0253	0.0489	−0.0289	−2.0	–	−25.8	99.7	237.7	13.1	97.9	–	12.6

within the accuracy of the predictions. This is according to expectations based on the relatively low Froude number and the small blocking factor in the towing tank for deep water conditions.

More differences between the solutions can be seen in Fig. 15, in which solutions for deep water and $\beta = 4°$ are given. The ReFRESCO and Star-CCM + results are very similar and differences can be attributed to the use of different grid resolutions, while close to the water surface some deviations are noticeable. In the ISIS-CFD results, the stern bilge vortex appears more pronounced and the wake contour lines at windward (port-side) are more curved.

Figure 16 shows wake fields for very shallow water and $\beta = 0°$. In shallow water, flow separation is detected, which is predicted by all computations. The wake is found to be thicker than in deep water. The most obvious difference between the computational results is the absence of the boundary layer on the bottom in the ISIS-CFD solution, due to the use of a free slip boundary condition. The Star-CCM + solution appears to have most flow separation, while the ReFRESCO result has least separation (smallest area with axial velocity $u/V < 0$). Furthermore, the location of the stern bilge vortex is slightly higher in the Star-CCM + prediction than in the other predictions.

Similar to the results for deep water, it is found that the influence of the free surface modelling and inclusion of trim and sinkage on the axial velocity fields predicted by ISIS-CFD is small, see Fig. 17. Of course, there is an influence on the integral quantities, as discussed previously.

In Fig. 18, the predictions for very shallow water and $\beta = 4°$ are shown. Compared to $\beta = 0°$, the area with flow separation has moved upward toward the windward (port side) and has reduced in size. Furthermore, the vortex generated at the starboard bilge is more pronounced than in deep water and is separated from the hull in very shallow water. Qualitative similarities are seen between the predictions, with the main difference being the absence of the boundary layer on the bottom in the ISIS-CFD solution, due to the use of a slip condition on this boundary. This probably also results in a slight difference in the strength and location of the starboard bilge vortex compared to the predictions obtained with the other solvers.

The wake fields for deep and very shallow water for $\gamma = 0.4$ are given in Fig. 19. Also in this case, the flow separation found at $\beta = 0°$ has moved upward towards the windward side and is reduced in strength.

7.2 Influence of water depth on the forces and moment

In Figs. 20 and 21 the influence of the water depth on the forces and moment is shown. For ReFRESCO the wide domain results are given, while for both other solvers the tank domain results are used. For Star-CCM + and ISIS-CFD the free surface calculations are shown. For $\beta = 4°$,

Table 11 Validation of resistance on different grids for $Re = 4.6 \times 10^6$ and $\beta = 0°$

Case	$X_f \times 10^2$	X_f (δ) (%)	$X_p \times 10^3$	$X \times 10^2$	X (E)(%)
KVLCC2 (bare)	ITTC: −1.410			−1.683	–
KVLCC2M ($Re = 4.6 \times 10^6$)	ITTC: −1.416	0.4		−1.707	1.4
ARS-DES-G1	−1.434	1.4	−2.993	−1.732	2.9
ARS-DES-G2	−1.432	1.3	−2.868	−1.719	2.1
ARS-DES-G3	−1.415	0.3	−2.980	−1.713	1.8
ARS-DES-G4	−1.377	−1.9	−2.879	−1.665	−1.1
ReFRESCO	−1.439	1.7	−3.032	−1.742	3.5

δ is %ITTC for X_f and E is %D

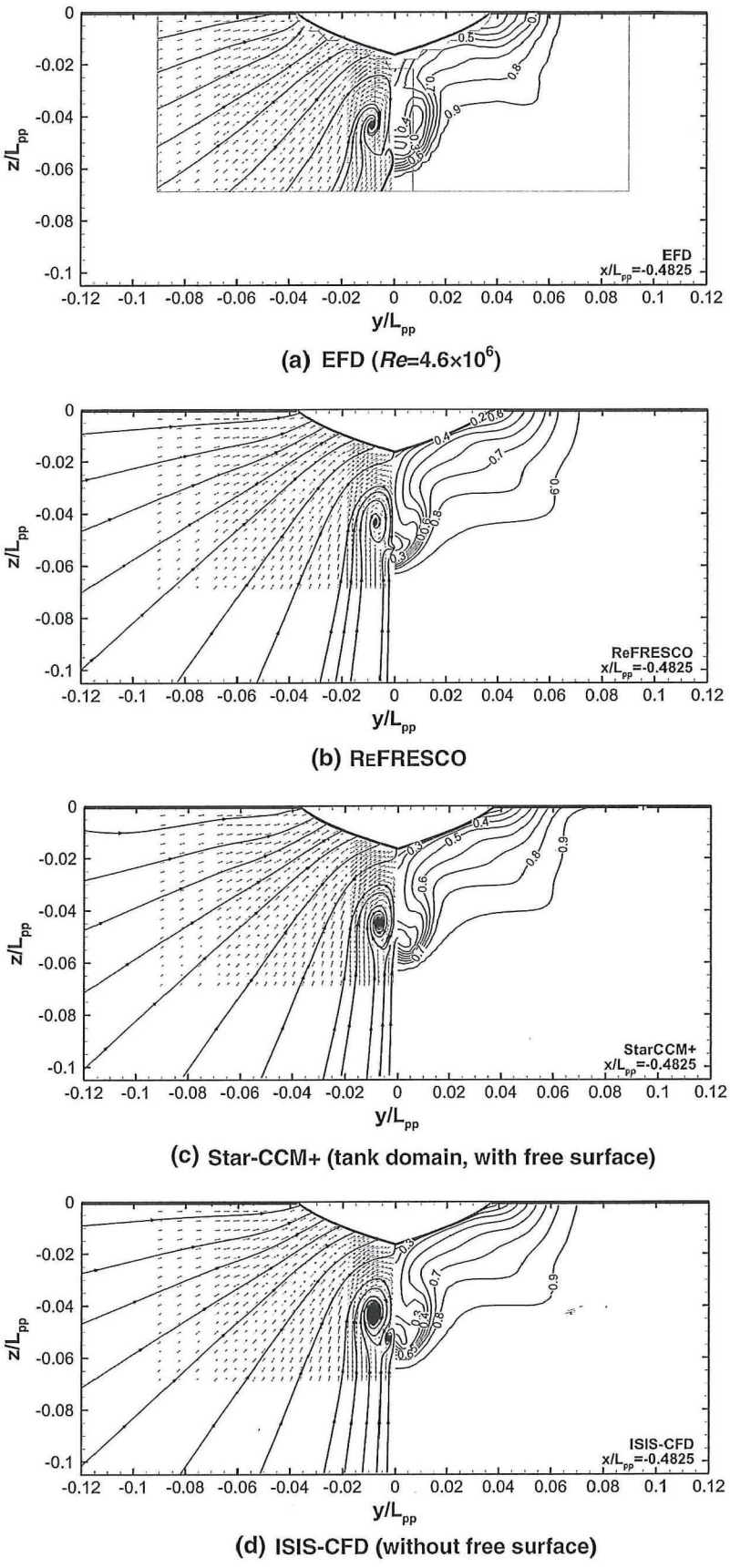

Fig. 13 Transverse (*left panel*) and axial wake (*right panel*), deep water, $\beta = 0°$, $x/L_{pp} = -0.4825$ (same results as in Fig. 11, but with enlarged axes ranges for comparison between water depths, drift angles and yaw rates)

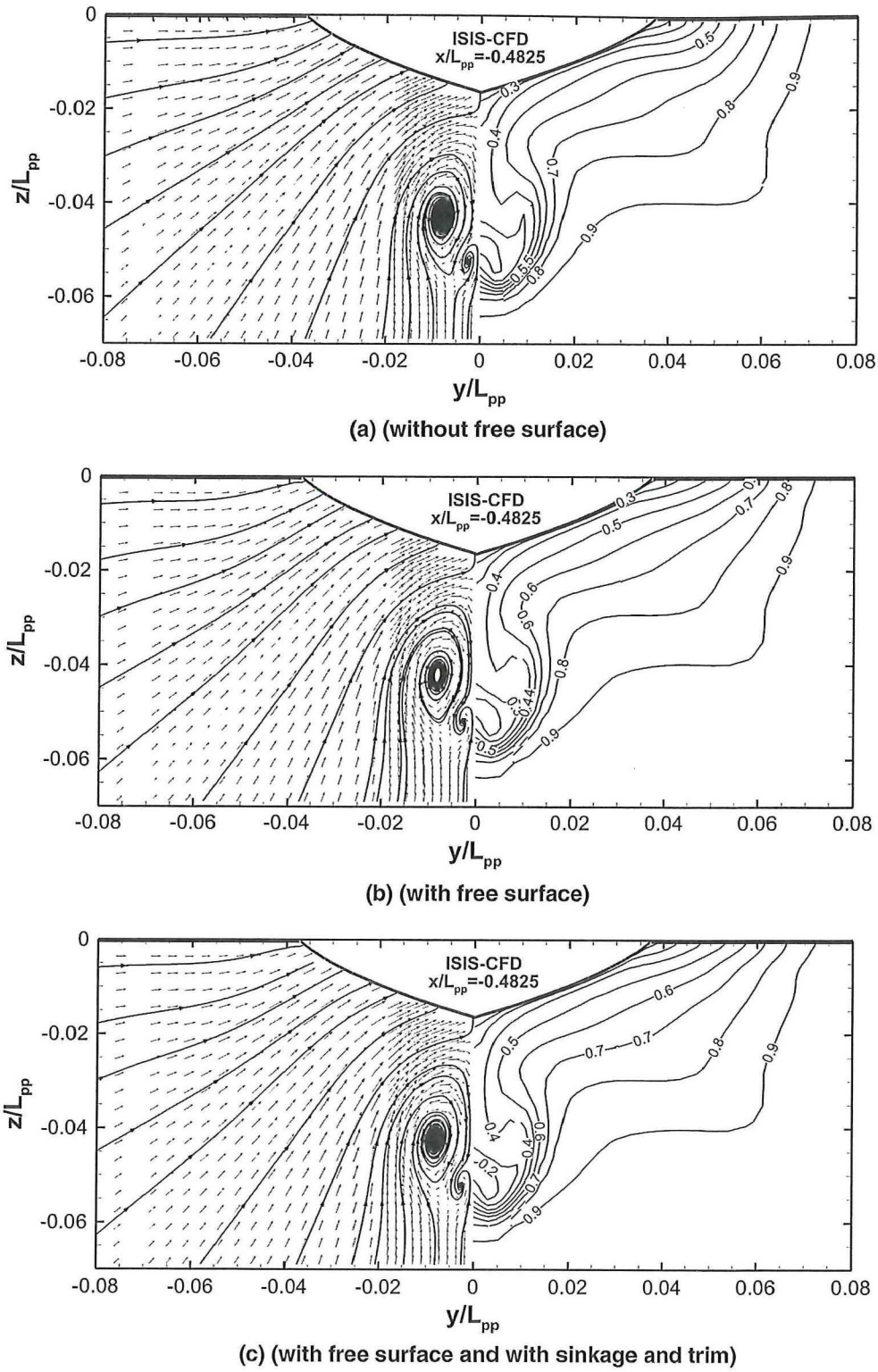

Fig. 14 Transverse (*left panel*) and axial wake (*right panel*), deep water, ISIS-CFD, $\beta = 0°$, $x/L_{pp} = -0.4825$

the ISIS-CFD solutions with free sinkage and trim are used. For some points, several experimental results are available from repeat tests, In those cases, all available points are included to illustrate possible scatter in the experiments. On the horizontal axes, the ratio $T/(h–T)$ is used, since with this representation the differences between the water depths can easily be distinguished. Low values of $T/(h–T)$ indicate deep water, while high values indicate shallow water. From these figures, it is found that the increase in resistance due to shallow water is underpredicted by

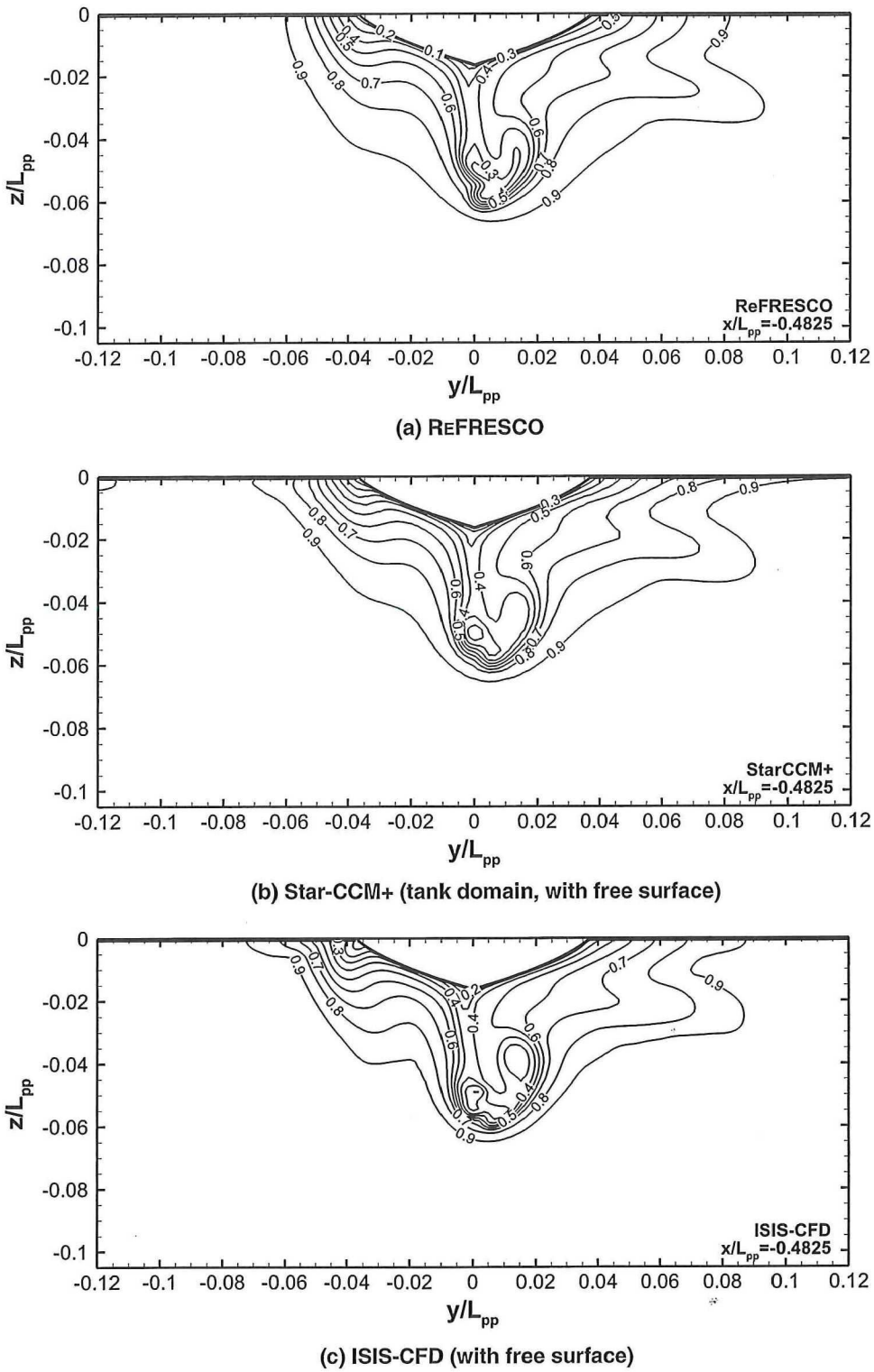

Fig. 15 Axial wake, deep water, $\beta = 4°$, $x/L_{pp} = -0.4825$

REFRESCO compared to Star-CCM + and ISIS-CFD, due to the neglect of the basin walls and the free surface. Generally, the predictions from Star-CCM + and ISIS-CFD are of the same order of magnitude, but the trends are not completely similar. This may be caused by uncertainties in the results or by the inclusion of sinkage and trim in the ISIS-CFD calculations.

The increase of the forces and moment in shallow water is considerable. For $\beta = 4°$, X increases by a factor of about 1.7, Y by about 6 and N by about 4. These values

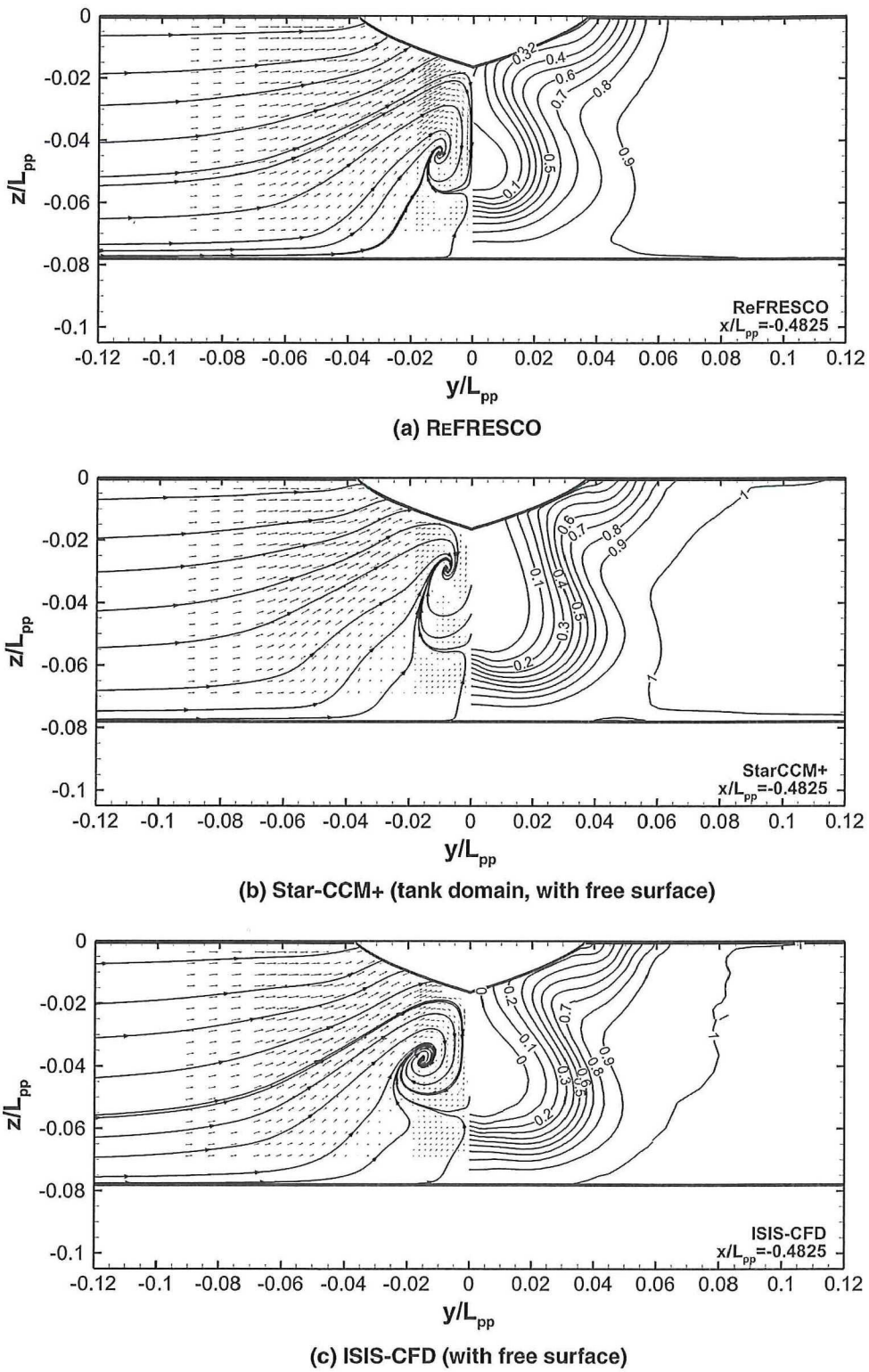

Fig. 16 Transverse (*left panel*) and axial wake (*right panel*), very shallow water, $\beta = 0°$, $x/L_{pp} = -0.4825$

correspond well with the general trends found for another tanker, the *Esso Osaka*, see Simonsen et al. [3], or results for the KVLCC2 by Zou [40]. Since Y increases more than N, the ratio N/Y, which is a measure for the instability of the ship, reduces. Together with the increase in N during yaw rate cases ($\gamma = 0.4$) this will lead to a more course-stable ship in shallow water than in deep water.

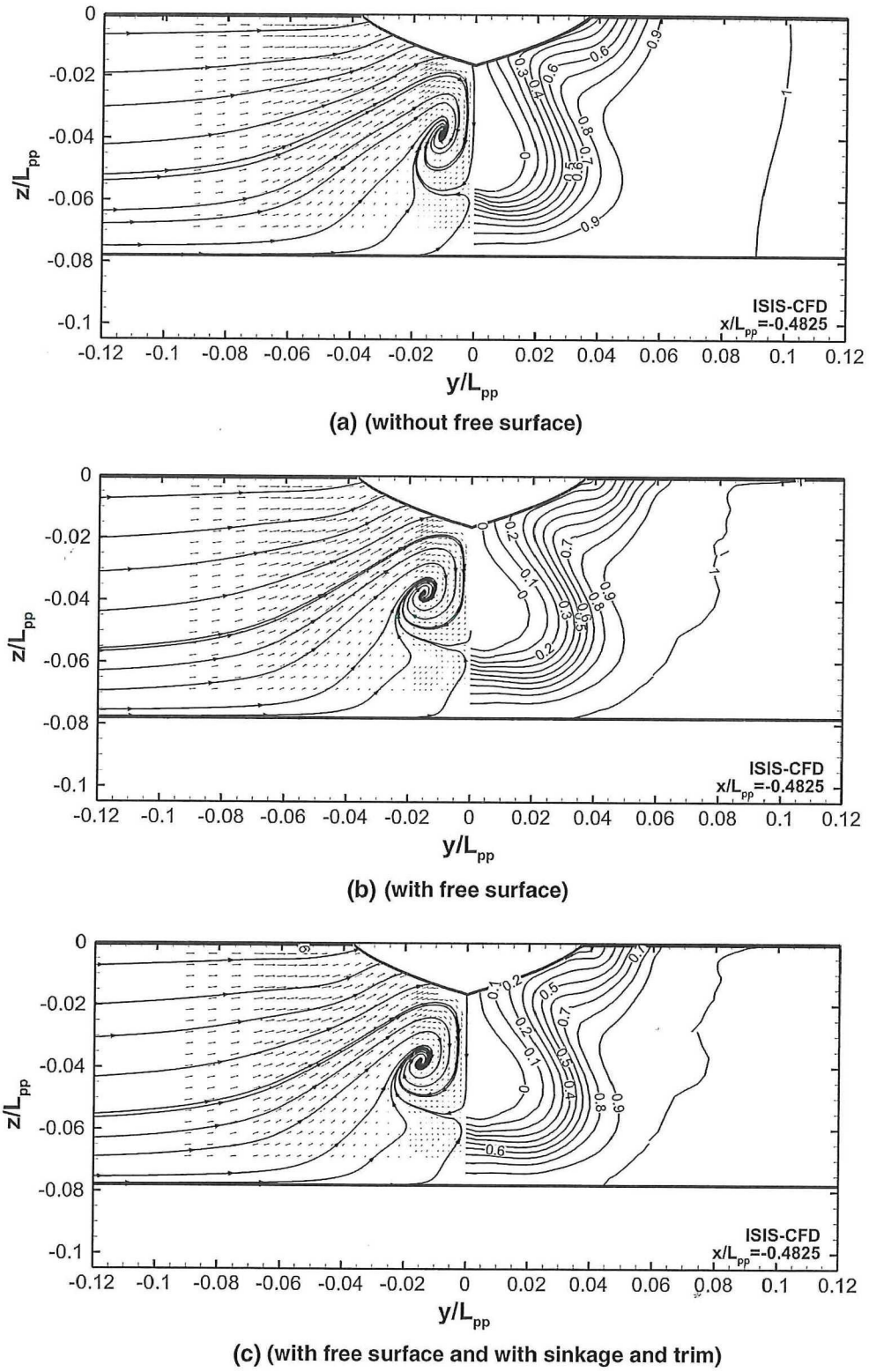

Fig. 17 Transverse (*left panel*) and axial wake (*right panel*), very shallow, ISIS-CFD, $\beta = 0°$, $x/L_{pp} = -0.4825$

8 Conclusions

The aim of this study is to assess the capability of CFD tools to accurately predict the forces and moments on manoeuvring ships and the associated flow fields and to determine the influence of different modelling choices, such as incorporation of basin walls, free surface or dynamic trim, on the trends in the results. Therefore, viscous-flow calculations have been conducted for a ship in manoeuvring conditions in deep and shallow water and the

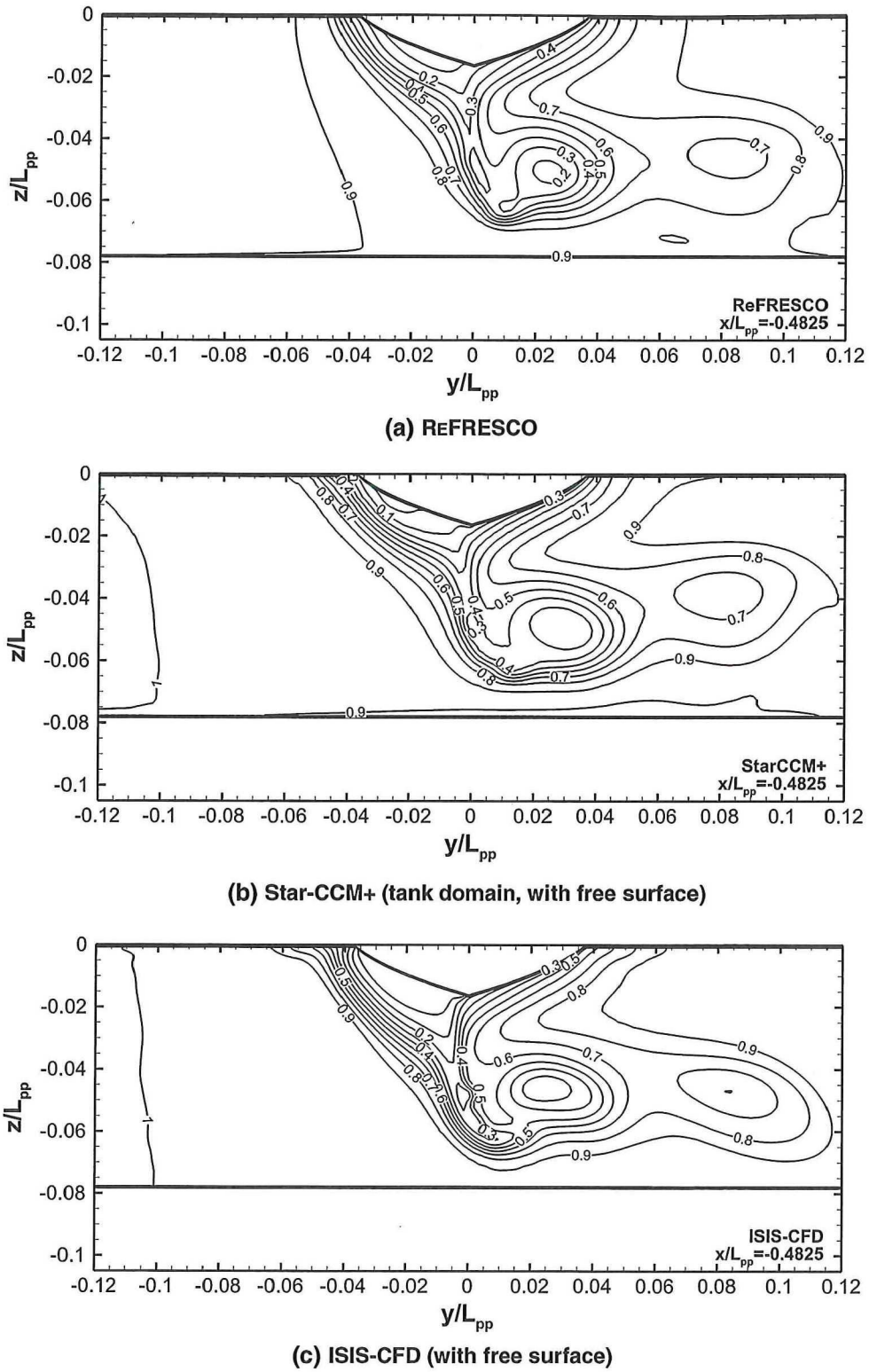

Fig. 18 Axial wake, very shallow water, $\beta = 4°$, $x/L_{pp} = -0.4825$

results are discussed in this article. Results from several different viscous-flow solvers are available. These solvers comprise commercial as well as bespoke codes.

Detailed verification and validation studies of the solutions have been conducted. The verification study shows that relatively fine grids are required to keep uncertainties within reasonable levels. Using grids without wall functions, densities below 1.6×10^6 will give unreliable results. Especially for the yaw rate case, large uncertainties are found and finer grids may be necessary.

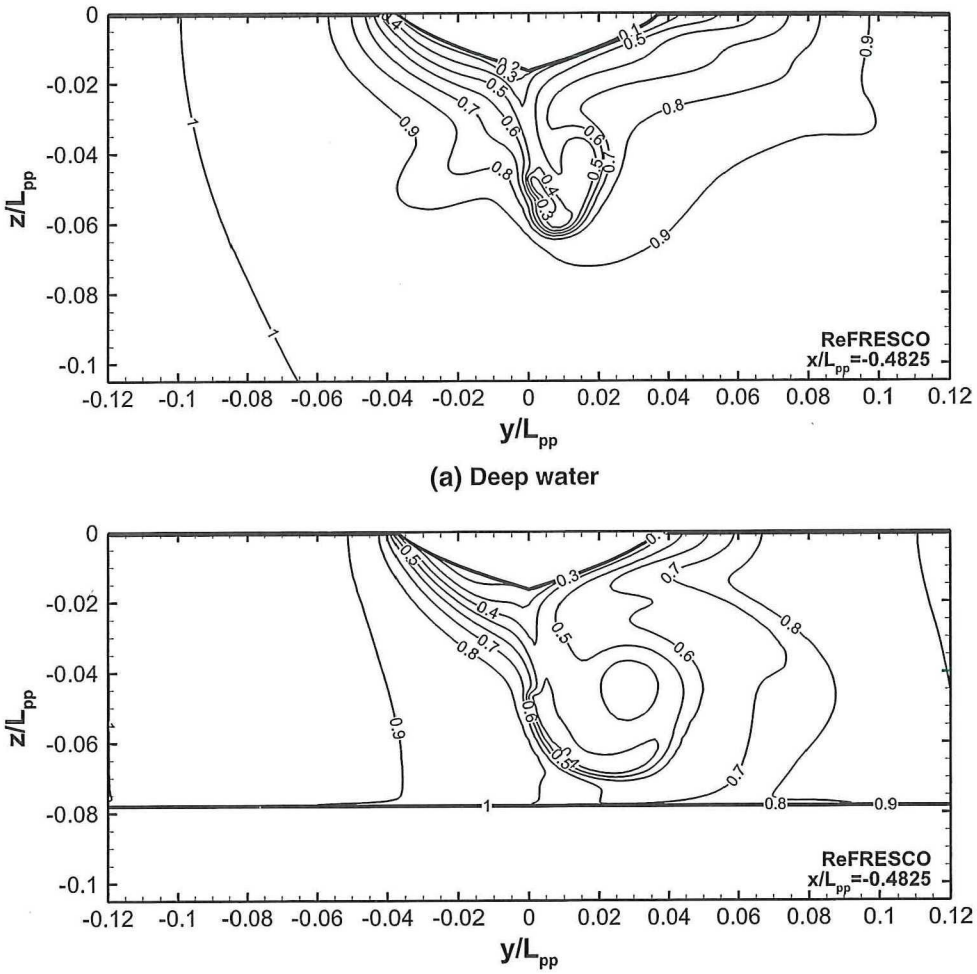

Fig. 19 Axial wake, ReFRESCO, $\gamma = 0.4$, $x/L_{pp} = -0.4825$

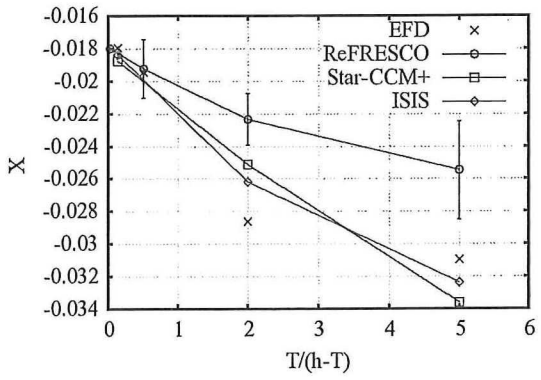

Fig. 20 Influence of water depth, $\beta = 0°$

Validation of the flow fields shows that turbulence modelling plays an important role in accurately predicting the wake of the ship. More advanced turbulence models such as EASM or ARS-DES produce wake fields with better resolution of the hook shape found in the experimental results. Comparing the predictions for deep and shallow water, it is seen that flow separation occurs during sailing at $\beta = 0°$ in shallow water. In manoeuvring conditions, this flow separation area moves toward the water surface and to the windward side, while reducing in strength. The influence of modelling the basin walls or free surface on the wake field is found to be small.

Concerning the integral quantities, validation of the resistance for straight ahead sailing in deep water is obtained at a level of about 6.5 $\%D$ compared to the INSEAN tests. Validation of additional resistance calculations is obtained at levels of about 3.7 $\%D$ of the resistance obtained during MOERI experiments. The validation uncertainties for these conditions are mainly governed by the uncertainty in the experimental results. For the other conditions, validation is not obtained for all results, indicating that modelling errors are present in some of the solutions. For the longitudinal force X, these can mainly be attributed to the neglect of the basin walls. The resistance increase due to the presence of the walls is about 10 %. This indicates that for validation of CFD for shallow water conditions the basin walls need to be modelled. On the other hand, the results also show

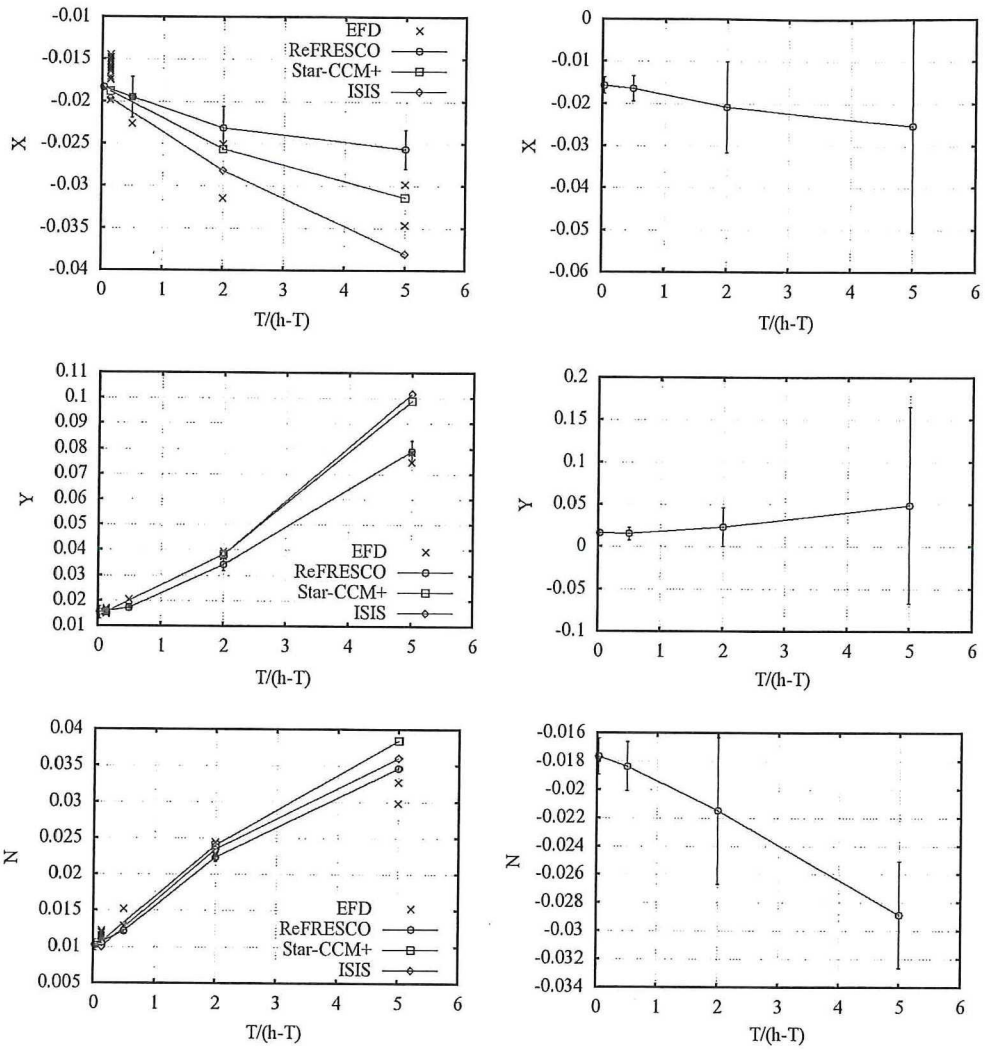

Fig. 21 Influence of water depth, $\beta = 4°$ and $\gamma = 0.4$

that in order to obtain correct resistance values for ships sailing in shallow water sufficiently wide basins are to be used for model tests. The influence of the basin walls on the transverse force Y and yaw moment N is also about 10 %. Comparison between the CFD results and the experiments shows that including the basin walls does not improve the comparison errors. Although uncertainties are not available and conclusions are therefore difficult to draw, this might be caused by the existence of a gap between the false bottom and the basin walls during the experiments. Such a gap will effectively reduce the blockage in the basin, which will be most pronounced in the most extreme shallow water conditions. Further examination of the experimental results is therefore recommended.

Calculations were conducted with and without modelling of the free surface deformation and some computations were done with free sinkage and trim. It appears that neglecting the free surface will under-estimate the forces by about 5 %. Neglecting the dynamic sinkage and trim of the ship does not change the results significantly at these conditions with very low Froude number.

The CFD calculations prove to be valuable in predicting the effect of shallow water on the forces and moments on a manoeuvring ship. Compared to deep water, X can increase by a factor 2, Y by 6 and N by 4. The trends found in this study correspond well to trends found by other authors or found during experiments with other ships.

Unfortunately, some doubts about the accuracy and uncertainty in the experimental results exist. Furthermore, the range of conditions considered during the tests is rather limited. Especially when manoeuvring at low speeds, with assistance of bow thrusters or tugs, drift angles or yaw rates will be much higher than those used during the tests. Therefore, obtaining new EFD data is a high priority for future research.

Acknowledgments Part of this research was sponsored by the US Office of Naval Research, Subaward P.O.No. 1000753759 (Prime Award No. N00014-10-C-0123) under administration of Dr. Patrick Purtell. The CFD simulations were conduced utilizing DoD HPC.

Appendix

Estimation of KVLCC2 bare hull resistance from experimental results

To estimate the resistance of the bare hull KVLCC2 at $Re = 4.6 \times 10^6$, the KVLCC2 with rudder data is corrected for the estimated resistance of the rudder. For this, the following steps are made:

First, the resistance R of the model is calculated (resistance coefficient based on wetted surface area $C_T = 4.11 \times 10^{-3}$ [5], with a specified uncertainty of $U_D = 1$ % [8]; wetted area with rudder $S_{wa} = 0.2682 \times L_{pp}^2$ [5]; model speed $V = 1.047$ m/s [8]):

$$\begin{aligned} R &= C_T \times 1/2 \times \rho \times V^2 \times S_{wa} \\ &= -4.11 \times 10^{-3} \times 0.5 \times 998 \times 1.047^2 \times 0.2682 \times L_{pp}^2 \\ &= 18.36 \text{ N} \end{aligned}$$

Then, the resistance of the rudder is estimated. For this, the average velocity at the rudder location is calculated, using a wake fraction of $w = 0.44$ [8]: $V_{rud} = (1 - w)V = 0.586$ m/s. The Reynolds number for the rudder with average chord $c = 0.149$ m follows from ($\nu = 1.256 \times 10^{-6}$ m^2/s based on the Reynolds number and model speed during the tests): $Re_{rud} = V_{rud}\, c/\nu = 6.96 \times 10^4$. Additionally, the rudder resistance coefficient is needed to calculate the rudder resistance. An estimate is made with the ITTC friction line, using an assumed form factor $(1 + k)$ of 1.1, which is reasonable for lifting surfaces:

$$C_{T,rud} \frac{0.075}{(\log(Re_{rud}) - 2)^2}(1 + k) = 10.21 \times 10^{-3}$$

The rudder wetted area follows from the difference between the wetted area with rudder and without rudder ($S_{wa,bare} = 0.2656 \times L_{pp}^2$ [39]), such that the rudder resistance is found:

$$\begin{aligned} R_{rud} &= C_{T,rud} \times 1/2 \times \rho \times V_{rud}^2 \times S_{wa,rud} \\ &= -10.21 \times 10^{-3} \times 0.5 \times 998 \times 0.586^2 \\ &\quad \times (0.2682 - 0.2656) \times L_{pp}^2 \\ &= 0.14 \text{ N} \end{aligned}$$

The non-dimensional longitudinal force X for the KVLCC2 without rudder is now estimated by:

$$X = -(R - R_{rud})/(1/2\rho V^2 L_{pp} T) = -1.683 \times 10^{-2}$$

Estimation of KVLCC2M bare hull resistance at $Re = 4.6 \times 10^6$ from experimental results

The resistance of the KVLCC2M can be scaled to a different Reynolds number using the form factor method. For this, the form factor is required, see also, e.g., Toxopeus [37]. In the Tokyo workshop, the form factor was specified to be: $(1 + k) = 1.2$ [39]. The total longitudinal force measured was given by Kume et al. [38]: $X = -1.756 \times 10^{-2}$, with $U_D = 3.3$ %. The friction coefficient for $Re = 3.945 \times 10^6$ leads to $X_f = -1.457 \times 10^{-2}$, using a wetted surface area of $S_{wa} = 0.2668 \times L_{pp}^2$ [39]. The residual resistance is therefore found as follows: $X_{res} = X - (1 + k) \cdot X_f = 0.76 \times 10^{-4}$. Taking the friction coefficient for $Re = 4.6 \times 10^6$, and combining this with the form factor and the residual resistance, the following longitudinal force is estimated for the KVLCC2M:

$$\begin{aligned} X &= (1 + k) \times X_f(Re = 4.6 \times 10^6) + X_{res} \\ &= 1.2 \times -1.416 \times 10^{-2} + 0.76 \times 10^{-4} \\ &= -1.707 \times 10^{-2} \end{aligned}$$

This value is about 1.4 % larger in magnitude than the estimated value for the KVLCC2 bare hull, which is within the uncertainty of the experiments.

References

1. Örnfelt M (2009) Naval mission and task driven manoeuvrability requirements for naval ships. In: 10th international conference on fast sea transportation (FAST). Athens, pp 505–518
2. Quadvlieg FHHA, Armaoğlu E, Eggers R, Coevorden P van (2010) Prediction and verification of the manoeuvrability of naval surface ships. In: SNAME Annual Meeting and Expo, Seattle/Bellevue, Washington
3. Simonsen CD, Stern F, Agdrup K (2006) CFD with PMM test validation for manoeuvring VLCC2 tanker in deep and shallow water. In: International conference on marine simulation and ship manoeuvring (MARSIM), Terschelling, The Netherlands
4. Larsson L, Stern F, Bertram V (2003) Benchmarking of computational fluid dynamics for ship flows: The Gothenburg 2000 workshop. J Ship Res 47(1):63–81
5. Larsson L, Stern F, Visonneau M (eds) (2010) Gothenburg 2010: a workshop on numerical ship hydrodynamics, Gothenburg
6. Stern F, Agdrup K (eds) (2008) SIMMAN workshop on verification and validation of ship manoeuvring simulation methods, Copenhagen
7. Lee S-J, Kim H-R, Kim W-J, Van S-H (2003) Wind tunnel tests on flow characteristics of the KRISO 3,600 TEU containership and 300k VLCC double-deck ship models. J Ship Res 47(1): 24–38
8. Kim W-J, Van S-H, Kim DH (2001) Measurement of flows around modern commercial ship models. Exp Fluids 31(5):567–578
9. Fabbri L, Benedetti L, Bouscasse B, Gala FL, Lugni C (2006) An experimental study of the manoeuvrability of a blunt ship: the effect of the water depth. In: International conference on ship and shipping research (NAV)
10. Fabbri L, Benedetti L, Bouscasse B, Gala FL, Lugni C (2006) An experimental study of the manoeuvrability of a blunt ship: the effect of the water depth. In: 9th numerical towing tank symposium (NuTTS)
11. Fabbri L, Campana E, Simonsen C (2011) An experimental study of the water depth effects on the KVLCC2 tanker. AVT-189 Specialists' Meeting, Portsdown West, UK, pp 12–14 October
12. Vaz G, Jaouen FAP, Hoekstra M (2009) Free-surface viscous flow computations. Validation of URANS code FreSCo. In: 28th

international conference on ocean, offshore and arctic engineering (OMAE), OMAE2009-79398, Honolulu, May 31–June 5
13. Vaz G, Waals O, Fathi F, Ottens H, Le Souef T, Kwong K (2009) Current Affairs—model tests, semi-empirical predictions and CFD computations for current coefficients of semi-submersibles. In: 28th international conference on ocean, offshore and arctic engineering (OMAE), OMAE2009-80216, Honolulu, May 31–June 5
14. Vaz G, Toxopeus SL, Holmes S (2010) Calculation of manoeuvring forces on submarines using two viscous-flow solvers. In: 29th international conference on ocean, offshore and arctic engineering (OMAE), OMAE2010-20373
15. Koop AH, Klaij CM, Vaz G (2010) Predicting wind shielding for FPSO tandem offloading using CFD. In: 29th international conference on ocean, offshore and arctic engineering (OMAE), OMAE2010-20284, Shanghai
16. Toxopeus SL (2011) Practical application of viscous-flow calculations for the simulation of manoeuvring ships. PhD thesis, Delft University of Technology, Faculty Mechanical, Maritime and Materials Engineering
17. Menter FR (1994) Two-equation eddy-viscosity turbulence models for engineering applications. AIAA J 32(8):1598–1605
18. Dacles-Mariani J, Zilliac GG, Chow JS, Bradshaw P (1995) Numerical/experimental study of a wingtip vortex in the near field. AIAA J 33:1561–1568
19. Bettle MC, Toxopeus SL, Gerber AG (2010) Calculation of bottom clearance effects on Walrus submarine hydrodynamics. Int Shipbuild Prog 57(3–4):101–125. doi:10.3233/ISP-2010-0065
20. StarCCM + User's manual
21. Queutey P, Visonneau M (2007) An interface capturing method for free-surface hydrodynamic flows. Comput Fluids 36(9):1481–1510. doi:10.1016/j.compfluid.2006.11.007
22. Duvigneau R, Visonneau M, Deng GB (2003) On the role played by turbulence closures in hull shape optimization at model and full scale. J Mar Sci Technol 8:11–25. doi:10.1007/s10773-003-0153-8
23. Deng GB, Visonneau M (1999) Comparison of explicit algebraic stress models and second order turbulence closures for steady flows around ships. In: 7th international conference on numerical ship hydrodynamics, Nantes, France
24. Leroyer A, Visonneau M (2005) Numerical methods for RANSE simulations of a self-propelled fish-like body. J Fluid Struct 20(3):975–991. doi:10.1016/j.jfluidstructs.2005.05.007
25. Xing T, Bhushan S, Stern F (2012) Vortical and turbulent structures for KVLCC2 at drift angle 0, 12, and 30 degrees. Ocean Eng 55:23–43. doi:10.1016/j.oceaneng.2012.07.026
26. Carrica PM, Wilson RV, Stern F (2007) An unsteady single-phase level set method for viscous free surface flows. Int J Numer Meth Fluids 53(2):229–256. doi:10.1002/fld.1279
27. Xing T, Shao J, Stern F (2007) BKW-RS-DES of unsteady vortical flow for KVLCC2 at large drift angles. In: 9th international conference on numerical ship hydrodynamics, Ann Arbor
28. International Organization for Standardization (ISO) (1995) Guide to the Expression of Uncertainty in Measurement
29. Stern F, Wilson RV, Coleman HW, Paterson EG (2001) Comprehensive approach to verification and validation of CFD simulations - part 1: methodology and procedures. J Fluids Eng 123(4):793–802. doi:10.1115/1.1412235
30. American Society of Mechanical Engineers (ASME) (2009) Standard for Verification and Validation in Computational Fluid Dynamics and Heat Transfer, V&V 20 Committee
31. Eça L, Vaz G, Hoekstra M (2010) A verification and validation exercise for the flow over a backward facing step. In: ECCOMAS fifth European conference on computational fluid dynamics, Lisbon, Portugal, June
32. Xing T, Stern F (2010) Factors of safety for Richardson extrapolation. J Fluids Eng. 132(6). doi: 10.1115/1.4001771
33. Coleman HW, Stern F (1997) Uncertainties in CFD code validation. J Fluids Eng 119(4):795–803. doi:10.1115/1.2819500
34. Bhushan S, Carrica P, Yang J, Stern F (2011) Scalability studies and large grid computations for surface combatant using CFDShip-Iowa. Int J High Perform Comput Appl 1–22. doi: 10.1177/1094342010394887
35. Xing T, Stern F (2011) Closure to discussion of: "factors of safety for Richardson extrapolation". J Fluids Eng 133(11): 115502. doi:10.1115/1.4005030
36. Larsson L, Stern F, Visonneau M (2011) CFD in ship hydrodynamics—results of the Gothenburg 2010 workshop. In: IV international conference on computational methods in marine engineering (MARINE), Lisbon
37. Toxopeus SL (2011) Viscous-flow calculations for KVLCC2 in deep and shallow water. In: IV international conference on computational methods in marine engineering (MARINE), Lisbon
38. Kume K, Hasegawa J, Tsukada Y, Fujisawa J, Fukasawa R, Hinatsu M (2006) Measurements of hydrodynamic forces, surface pressure, and wake for obliquely towed tanker model and uncertainty analysis for CFD validation. J Mar Sci Technol 11(2):65–75. doi:10.1007/s00773-005-0209-y
39. Hino T (ed) (2005) CFD Workshop Tokyo 2005, Tokyo
40. Zou L (2011) CFD predictions including verification and validation of hydrodynamic forces and moments on a ship in restricted waters. Licentiate thesis, Chalmers University of Technology, Gothenburg, Sweden